



THE HONG KONG
POLYTECHNIC UNIVERSITY

香港理工大學

Pao Yue-kong Library

包玉剛圖書館

Copyright Undertaking

This thesis is protected by copyright, with all rights reserved.

By reading and using the thesis, the reader understands and agrees to the following terms:

1. The reader will abide by the rules and legal ordinances governing copyright regarding the use of the thesis.
2. The reader will use the thesis for the purpose of research or private study only and not for distribution or further reproduction or any other purpose.
3. The reader agrees to indemnify and hold the University harmless from and against any loss, damage, cost, liability or expenses arising from copyright infringement or unauthorized usage.

IMPORTANT

If you have reasons to believe that any materials in this thesis are deemed not suitable to be distributed in this form, or a copyright owner having difficulty with the material being included in our database, please contact lbsys@polyu.edu.hk providing details. The Library will look into your claim and consider taking remedial action upon receipt of the written requests.

THEORETICAL STUDY OF TOPOLOGICAL GYROTROPIC LATTICES
WITH DYNAMIC LONG-RANGE INTERACTIONS

WU PAK HONG RAYMOND

PhD

The Hong Kong Polytechnic University

2020

The Hong Kong Polytechnic University

Department of Applied Physics

Theoretical Study of Topological Gyrotropic Lattices with
Dynamic Long-range Interactions

A thesis submitted in partial fulfilment of the requirements for
the degree of Doctor of Philosophy

WU Pak Hong Raymond

June 2019

CERTIFICATE OF ORIGINALITY

I hereby declare that this thesis is my own work and that, to the best of my knowledge and belief, it reproduces no material previously published or written, nor material that has been accepted for the award of any other degree or diploma, except where due acknowledgement has been made in the text.

_____ (Signed)

WU Pak Hong Raymond (Name of student)

Abstract

Topological photonics have been of great interest for the past decade, as the topological edge modes were proven to be robust against local perturbations. In this thesis, we study one-dimensional (1D) topological gyrotropic lattices beyond the Su-Schrieffer-Heeger (SSH) model. Different from the conventional SSH model that has only nearest-neighbor interactions, we consider, in general, dispersive systems with dynamic long-range interactions. The electromagnetic resonances of both gyroelectric lattices and gyromagnetic lattices are studied and compared. We find that the normal modes of the system coupled strongly to the photon mode of the background medium. In particular, the dynamic effects create a different band gap in gyromagnetic systems. We propose a 1D topological model for such a dispersive gyromagnetic system and demonstrate that the dynamic long-range interaction can lead to localized topological edge modes, while the quasi-static interaction alone does not. Our results indicate that the dynamic long-range interaction plays a crucial role in predicting the precise band structures and the spectral position of the topological edge modes in strongly dispersive gyrotropic

systems, which deepen our understanding on the topology in non-reciprocal photonics.

Acknowledgments

First of all, I would like to thank my supervisors, Dr. Kin Hung FUNG and Prof. Siu Fung YU, for giving me an opportunity to be their student. I wish to express my special thanks to Dr. Kin Hung FUNG for his guidance. I learnt a lot from him. I am greatly in debt to him for his advice and support.

I would like to thank the professors who taught me physics during my study. I would also like to thank all the people who have been members of Dr. Kin Hung FUNG's research group for their help.

I would like to thank my friends and family. I wish to thank my parents for their continuous supports. Finally, thank you to Sze Wa CHAN for all her love and encouragement.

Contents

Contents	v
List of Figures	vii
1 Introduction	1
1.1 Arrays of subwavelength particles	1
1.2 Topological photonics	3
1.3 The Su-Schrieffer-Heeger (SSH) model	4
1.4 Beyond the SSH model	6
1.5 Structure of this thesis	7
2 Theory	9
2.1 Coupled-dipole method in two dimensions	9
2.2 Coupled-dipole method in three dimensions	12
2.3 Lattice sums for the 3D Green's tensor	13
2.4 Eigen-response theory	18
2.5 Zak phase and bulk-boundary correspondence	19

<i>CONTENTS</i>	vi
3 One-dimensional (1D) gyromagnetic lattices	22
3.1 Regular chain	24
3.1.1 Infinite lattice	24
3.2 Dimerized chain	33
3.2.1 Model	33
3.2.2 Topological phase transition	36
3.2.3 Finite lattice and topological edge modes	38
4 One-dimensional (1D) gyroelectric lattices	49
4.1 Regular chain	49
4.1.1 Infinite lattice	49
4.2 Dimerized chain	60
4.2.1 Model	60
4.2.2 Finite lattice and topological edge modes	65
Conclusions	75
A Coupled-dipole equations in quasi-static limit	77
B Coupled-dipole equations for the dimer model in quasi-static limit	80
C Finite gyromagnetic lattice in quasi-static limit	82
References	85

List of Figures

1.1	Illustration of the SSH model. The lattice constant is given by a_2 . The unit cell is indicated by the dashed box. The distance between cylinder A and cylinder B is given by b	5
3.1	Illustration of gyromagnetic cylinders on 1D infinite lattice. The lattice constant is given by a_1 . The unit cell is indicated by the dashed box.	22
3.2	(a) The photonic band structure with short- and long-range interactions in quasi-static limit. The blue line is the dispersion relation with nearest-neighbor interactions only. (b) The photonic band structure with dynamic long-range interactions. The white dotted lines are the light lines and the region within the light lines is the light cone. The cyan dashed line indicates the resonant frequency of a single gyromagnetic cylinder ω_0	23

- 3.3 Illustration of dimer model of gyromagnetic cylinders on 1D infinite lattice. The lattice constant is given by a_2 . The unit cell is indicated by the dashed box. The distance between cylinder A and cylinder B is given by $b = (1 - \delta)a_2/2$ 31
- 3.4 (a), (b), (c), (d) The photonic band structure for dimer model in quasi-static limit and in general, with dynamic effects. All results include the long-range interactions. The white dotted lines are the light lines and the region within the light lines is the light cone. The cyan dashed line indicates the resonant frequency of a single gyromagnetic cylinder ω_0 32
- 3.5 Band inversion and topological phase transition in dimer model of gyromagnetic cylinders on 1D infinite lattice. The curves are the upper and lower band edges at $k = \pi/a_2$ and the grey areas are the band gap. The eigenstate of the unit cell with $\delta = 0.2$ and $\delta = -0.2$ for both upper band and lower band are illustrated. The in-phase eigenmodes and the corresponding band are in blue, while the anti-phase eigenmodes and the corresponding band are in red. The cyan dashed line indicates the resonant frequency of a single gyromagnetic cylinder ω_0 . For $\delta < 0$, the system is in topological phase I, while for $\delta > 0$, it is in topological phase II. At $\delta = 0$, the system is gapless, which undergoes band inversion and topological phase transition. . . 37

3.6 Illustration of 1D topological model of gyromagnetic lattices. The lattice constant is given by a_2 . The finite lattice composed of a left and a right part with different unit cells. The unit cells are indicated by the dashed boxes and indexed by the integer n . The distance between cylinder A and cylinder B , in the left and the right part of the lattice, is given by $b_L = (1 - \delta_L)a_2/2$ and $b_R = (1 - \delta_R)a_2/2$, respectively. 38

3.7 Band structures of dimer model of gyromagnetic cylinders on 1D finite lattice. (a) The topologically trivial system with both $\delta_L = 0.2$ and $\delta_R = 0.2$. (b) The topologically non-trivial system with both $\delta_L = -0.2$ and $\delta_R = -0.2$. (c) The system with $\delta_L = 0.2$ and $\delta_R = -0.2$, where the left and the right part of the lattice are topologically trivial and non-trivial, respectively. The upper and the lower triangle indicate the upper and the lower bands, respectively. The circle and the square are the topological edge modes. The cyan dashed line indicates the resonant frequency of a single gyromagnetic cylinder ω_0 39

3.8 The norm of eigenmodes corresponding to the labeled modes in the band structures in Fig. 3.7. (a), (b), (c) The results for the system with $\delta_L = -0.2$ and $\delta_R = -0.2$. (d), (e), (f), (g) The results for the system with $\delta_L = 0.2$ and $\delta_R = -0.2$. In particular, (c), (e), and (f) are topological edge modes. 40

3.9 The norm of eigenmodes in semi-log plot corresponding to the labeled modes in the band structures in Fig. 3.7. (a), (b), (c) The results for the system with $\delta_L = -0.2$ and $\delta_R = -0.2$. (d), (e), (f), (g) The results for the system with $\delta_L = 0.2$ and $\delta_R = -0.2$. In particular, (c), (e), and (f) are topological edge modes. 41

3.10 Topological phase transition of dimer model of gyromagnetic cylinders on 1D finite lattice with $\delta_L = 0.2$ and $\delta_R \in [-0.2, 0.2]$. The white dashed line at $\delta_R = 0$ indicates topological phase transition in the right part of the lattice and the cyan dashed line indicates the resonant frequency of a single gyromagnetic cylinder ω_0 . The blue square and the blue circle are the topological edge modes. 42

4.1 Illustration of gyroelectric cylinders on 1D infinite lattice. The lattice constant is given by a_1 . The unit cell is indicated by the dashed box. The size of the gyroelectric system is 10^4 times smaller than the gyromagnetic one considered in Chapter 3. 50

4.2 The splitting of resonant frequency of a single gyroelectric cylinder ω_0 in the presence of applied static magnetic field B . The blue dotted line indicated the resonant frequency $\omega_0 = \omega_p/\sqrt{2}$ for $B = 0$. Two two blue lines correspond to the splitted resonant frequency $\omega_{0,+}$ and $\omega_{0,-}$ 51

4.3 (a) The photonic band structure with short- and long-range interactions in quasi-static limit. The blue and red lines are the dispersion relation with nearest-neighbor interactions only. (b) The photonic band structure with dynamic long-range interactions. The white dotted lines are the light lines and the region within the light lines is the light cone. The cyan dashed line indicates the resonant frequency of a single gyroelectric cylinder $\omega_{0,\pm}$. All results are calculated with $B = 0.5$ T. 52

4.4 Illustration of dimer model of gyroelectric cylinders on 1D infinite lattice. The lattice constant is given by a_2 . The unit cell is indicated by the dashed box. The distance between cylinder A and cylinder B is given by $b = (1 - \delta)a_2/2$. The size of the gyroelectric system is 10^4 times smaller than the gyromagnetic one considered in Chapter 3. 60

4.5 (a), (b), (c), (d) The photonic band structure for dimer model with $B = 0.5$ T in quasi-static limit and in general, with dynamic effects. All results include the long-range interactions. The white dotted lines are the light lines and the region within the light lines is the light cone. The cyan dashed line indicates the resonant frequency of a single gyroelectric cylinder $\omega_{0,\pm}$ 61

- 4.6 The normal modes in the dimerized chain. The photonic band structure for dimer model with dynamic long-range interactions. The eigenstate of the unit cell for each band is illustrated. The in-phase eigenmodes are in blue, while the anti-phase eigenmodes are in red. The white dotted lines are the light lines and the region within the light lines is the light cone. The cyan dashed line indicates the resonant frequency of a single gyroelectric cylinder $\omega_{0,\pm}$ 62
- 4.7 Illustration of 1D topological model of gyroelectric lattices. The lattice constant is given by a_2 . The finite lattice composed of a left and a right part with different unit cells. The unit cells are indicated by the dashed boxes and indexed by the integer n . The distance between cylinder A and cylinder B , in the left and the right part of the lattice, is given by $b_L = (1-\delta_L)a_2/2$ and $b_R = (1-\delta_R)a_2/2$, respectively. The size of the gyroelectric system is 10^4 times smaller than the gyromagnetic one considered in Chapter 3. 65
- 4.8 Band structures of dimer model of gyroelectric cylinders on 1D finite lattice with $B = 0.5$ T. (a) The topologically trivial system with both $\delta_L = 0.2$ and $\delta_R = 0.2$. (b) The same band structure in high resolution. The cyan dashed line indicates the resonant frequency of a single gyroelectric cylinder $\omega_{0,\pm}$ 66

4.9 Band structures of dimer model of gyroelectric cylinders on 1D finite lattice with $B = 0.5$ T. (a) The topologically non-trivial system with both $\delta_L = -0.2$ and $\delta_R = -0.2$. (b) The same band structure in high resolution. The upper and the lower triangle indicate the upper and the lower bands, respectively. The circles are the topological edge modes each with two-fold degeneracy. The cyan dashed line indicates the resonant frequency of a single gyroelectric cylinder $\omega_{0,\pm}$ 67

4.10 The norm of eigenmodes corresponding to the labeled modes in the band structures in Fig. 4.9. The results for the system with $\delta_L = -0.2$ and $\delta_R = -0.2$. (a), (f) are the upper and the lower bands, respectively. (b), (c), (d), (e) are topological edge modes and each of them has two-fold degeneracy. 68

4.11 Band structures of dimer model of gyroelectric cylinders on 1D finite lattice with $B = 0.5$ T. (a) The system with $\delta_L = 0.2$ and $\delta_R = -0.2$, where the left and the right part of the lattice are topologically trivial and non-trivial, respectively. (b) The same band structure in high resolution. The upper and the lower triangle indicate the upper and the lower bands, respectively. The circles and the squares are the topological edge modes. The cyan dashed line indicates the resonant frequency of a single gyroelectric cylinder $\omega_{0,\pm}$ 69

4.12 The norm of eigenmodes corresponding to the labeled modes in the band structures in Fig. 4.11. The results for the system with $\delta_L = 0.2$ and $\delta_R = -0.2$. (a), (f) are the upper and the lower bands, respectively. (b), (c), (d), (e) are topological edge modes. 70

C.1 Band structures of dimer model of gyromagnetic cylinders on 1D finite lattice in quasi-static limit. (a) The system with both $\delta_L = 0.2$ and $\delta_R = 0.2$. (b) The system with both $\delta_L = -0.2$ and $\delta_R = -0.2$. (c) The system with $\delta_L = 0.2$ and $\delta_R = -0.2$. The cyan dashed line indicates the resonant frequency of a single gyromagnetic cylinder ω_0 83

C.2 The norm of the localized eigenmodes corresponding to the band structures in Fig. C.1. (a) The results for the system with $\delta_L = -0.2$ and $\delta_R = -0.2$ at $\omega = 24.2112 \times 10^9 \text{ rad s}^{-1}$. (b), (c) The results for the system with $\delta_L = 0.2$ and $\delta_R = -0.2$ at $\omega = 24.2112 \times 10^9 \text{ rad s}^{-1}$ and $\omega = 24.2096 \times 10^9 \text{ rad s}^{-1}$. . . 84

Chapter 1

Introduction

1.1 Arrays of subwavelength particles

The ability to control light is always challenging and leads to important applications. Arrays of subwavelength particles, such as plasmonic nanoparticles and dielectric nanoparticles have attracted a lot of interests due to the interesting possibilities for potential applications in manipulating electromagnetic waves. Comparing to photonic crystals, array of subwavelength particles use less materials and are more compact in size.

In particular, one-dimensional (1D) arrays of plasmonic nanoparticles have been intensively studied due to their abilities of guiding and confining light in the nanoscale[1, 2, 3, 4, 5]. The guided modes in arrays of plasmonic nanoparticles are due to the interactions of localized plasmons in the plasmonic nanoparticles. Many properties of the plasmonic nanoparticles can be

studied analytically under the dipole approximation, where each nanoparticles can be treated as a point dipole, and the operating frequency of devices based on such arrays of plasmonic nanoparticles are in the terahertz regime.

Recently, arrays of gyromagnetic subwavelength particles operating microwave regime have also been studied[6, 7]. The gyromagnetic particles can be studied with a similar dipole model, where the electric dipoles in plasmonic nanoparticles is analog to a magnetic dipoles in gyromagnetic particles. In gyromagnetic media, the magnetization not only breaks both the time reversal symmetry and the Lorentz reciprocity due to the non-symmetric permeability tensor $\boldsymbol{\mu} \neq \boldsymbol{\mu}^T$, but it also breaks other spatial symmetries. System with broken symmetries and Lorentz reciprocity have possibility to support unidirectional light propagation and can form the basis for designing metasurfaces[8]. This has important applications in optical information technology, such as overcoming time-bandwidth limit[9], optical isolator[10], and optical circulator[11]. It is found that, arrays of gyromagnetic subwavelength particles can be useful in power transmission, where Faraday rotation is observed[6] and self-guided unidirectional waveguides can be realized[7].

Apart from gyromagnetic particles, an analog system can be obtained when external magnetic field is applied to array of plasmonic nanoparticles. The magnetized plasmon, or gyroelectric, systems with non-symmetric permittivity tensor $\boldsymbol{\epsilon} \neq \boldsymbol{\epsilon}^T$ were proven to present Faraday rotation[12] and non-reciprocal propagation of electromagnetic waves[13]. As we seen, both gyromagnetic and gyroelectric particles, or simply known as gyrotropic par-

ticles are very useful and interesting. In this thesis, we study arrays of gyrotropic subwavelength particles together with the concept of topology which will be introduced in the subsequent chapters.

1.2 Topological photonics

In the past decade, topological photonics[14, 15] has become a rapidly growing field of research since the analogs of quantum Hall edge states were theoretically proposed[16, 17, 18] and experimentally realized[19] in two-dimensional (2D) gyromagnetic photonic crystals. The bulk-boundary correspondence predicts edge modes existing at the boundary between systems with distinct topological phases, which are backscattering-immune and robust against local perturbations[14, 15]. Topological edge modes can be supported in many photonic systems, such as coupled resonator arrays[20, 21, 22], bi-anisotropic metamaterials[23], photonic crystals made of dielectric cylinders[24], radio-frequency circuits[25], cavity and circuit quantum electrodynamics systems[26, 27], and three-dimensional Weyl points and nodal lines systems[28] or in even higher synthetic dimensions[29, 30]. The enhanced light-matter interactions associated with topological edge modes may lead to many potential applications, such as efficient and robust lasers[31, 32, 33, 34, 35, 36].

Recently, it has been shown that topological modes can be realized in one-dimensional (1D) photonic crystals[37, 38], and 1D arrays of plasmonic[39, 40,

41, 42, 43, 44, 45] and dielectric nanoparticles[46, 47, 48]. In particular, the Majorana states are found in the zigzag chains of plasmonic nanoparticles[39] and lasing topological edge states are reported in the photonic analogs of Su-Schrieffer-Heeger (SSH) model[31, 33, 34].

Since the rise of topological photonics, there have been extensive study on the topological edge modes in gyromagnetic systems including continuous media[49, 50] and 2D lattices[17, 19, 51, 52, 53, 54]. Previously, 1D gyromagnetic lattices have been studied either with a focus on high frequency modes[7], or in quasi-static limit with short-range interactions[6]. Compare to 2D systems, there is lack of work in 1D topological gyromagnetic systems, and the same is also true for 1D topological gyroelectric system, even their analogs of the simplest SSH model, if exists, have not been discussed. This gives the motivation of this work to clarify the topological physics in these non-reciprocal photonic systems.

1.3 The Su-Schrieffer-Heeger (SSH) model

In 1979, the theoretical study of soliton formation in long-chain polyenes leads to the famous Su-Schrieffer-Heeger (SSH) model[55]. The SSH model describing spinless fermions hopping on a 1D lattice with staggered hopping amplitudes is one of the simplest systems exhibiting non-trivial topological bands. Although the SSH model is simple, it captures all the topological physics of 1D systems. The details of the topological invariant, bulk-

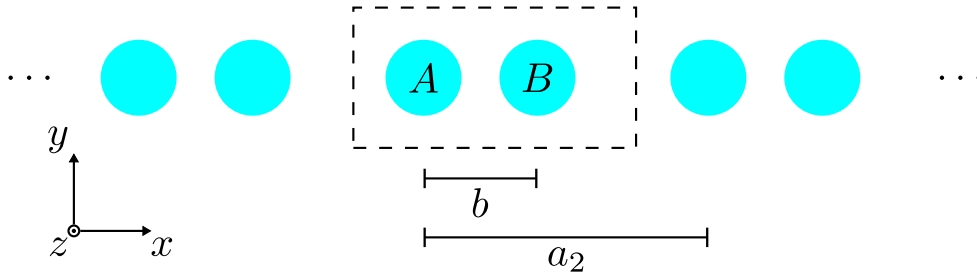


Figure 1.1: Illustration of the SSH model. The lattice constant is given by a_2 . The unit cell is indicated by the dashed box. The distance between cylinder A and cylinder B is given by b .

boundary correspondence, and topological edge modes for 1D systems will be discussed in Chapter 2. The SSH model is essentially a dimerized chain on a 1D lattice, as depicted in Fig. 1.1. The unit cell consists of two particles, labeled as A and B , and the displacement from particle A to particle B is given by b . It is a universal model and the analogs of the SSH model appear in many different physical systems. The model is studied using a tight-binding approach with only nearest-neighbor interactions being considered. In photonic systems, it is usually studied in quasi-static limit. It is known that the SSH model under these approximations exhibit chiral symmetry[56]. In short, we say a system with Hamiltonian \hat{H} has chiral symmetry, if $\hat{\Gamma}\hat{H}\hat{\Gamma}^\dagger = -\hat{H}$, where $\hat{\Gamma}$ is an operator. The chiral symmetry operator has to be unitary and Hermitian, which can be written succinctly as $\hat{\Gamma}^\dagger\hat{\Gamma} = \hat{\Gamma}^2 = 1$. The characteristics of the SSH model that are most interested to us is the consequences of chiral symmetry for energy eigenstates. The spectrum of a chiral symmetric Hamiltonian is symmetric. For any state with energy E , there is a chiral symmetric partner with energy $-E$, and the

edge state lies at the zero-energy state. This was validated in a variety of analogous photonic systems under the tight-binding approach[46, 40, 48].

1.4 Beyond the SSH model

As mentioned in Chapter 1.3, a tight-binding approach is widely used in studying the topology of bands in photonic systems. In that approach, the systems are studied in quasi-static limit with only short-range interactions being considered. Under these approximations, the retardation and radiative effects, or simply the dynamic effects, is neglected.

Recently, however, we demonstrated that dynamic long-range interactions play a crucial role in the accurate prediction of the photonic band structures and topological edge modes in the SSH and nonsymmorphic Rice-Mele model of plasmonic nanoribbon lattices[43]. Our observations are confirmed in the subsequent investigations of plasmonic nanoparticles chains in both classical[44] and quantum regime[45]. Different from the electron wave functions, the electromagnetic fields of photonic resonators are not very localized. Although the near fields are stronger than the far fields, the effects of the far fields can play an important role in some circumstance. In that case, long-range interactions and dynamic effects cannot be neglected, otherwise some interesting physics may be overlooked[43, 44, 45].

Moreover, many works in topological photonics assume a non-dispersive and focus on Hermitian systems[17, 20]. In principle, photonic systems are

inherently dispersive. Furthermore, even if damping is neglected, the systems are still non-Hermitian in nature due to the retardation and radiative effects. It is found that non-Hermitian due to dynamic long-range interactions can have interesting topology[44].

In the present work, we investigate the effects of dynamic long-range interactions on the photonic band structures and the topological edge modes in 1D arrays of dispersive gyrotropic resonators beyond the SSH model. We use the eigen-response theory[57, 58, 4, 59], which will be introduced in Chapter 2 and was extensively used in the studying of coupled plasmonic resonators, to account for the dynamic long-range interactions and, meanwhile, to create mapping to a non-Hermitian eigenvalue problem.

1.5 Structure of this thesis

In this chapter, the background of 1D topological photonics has been reviewed. The motivation and objective of this work are stated. In Chapter 2, the theory underlying this work is introduced. The coupled-dipole method and the eigen-response theory in 2D space for multiple dispersive gyrotropic cylinders is formulated. Also, the Zak phase and bulk-boundary correspondence for 1D topological systems is reviewed. In Chapter 3, the results for 1D gyromagnetic lattices are presented. The band structures of a regular chain and a dimerized chain are calculated, which demonstrated the importance of dynamic long-range interactions. Then topological phase transition

in a dimerized chain is discussed and topological edge modes supporting in a finite lattice is demonstrated. In Chapter 4, the results for 1D gyroelectric lattices are presented. The structure of this chapter is analog to Chapter 3. The objective of this chapter is to show the difference between gyroelectric lattices and gyromagnetic lattices. Finally, the conclusions of this thesis is given in Chapter 5.

Chapter 2

Theory

In this chapter, we formulate the theory in 2D space underlining the work of this thesis. We will be focusing on the magnetic phenomena associated with gyromagnetic system. Then, by the duality of Maxwell's equation, all the equations formulated can be transformed to their electric counterparts associated with gyroelectric system. It should be noted that, Gaussian units are used in this chapter. Furthermore, we assume and follow the convention for the time dependence $e^{-i\omega t}$.

2.1 Coupled-dipole method in two dimensions

In this section, we describe the coupled-dipole method in two dimensions for multiple dispersive gyromagnetic cylinders. Coupled-dipole method is used extensively in studying electromagnetic interactions between multiple

particles, such as arrays of plasmonic and dielectric nanoparticles.

We begin by considering multiple cylinders in the xy -plane. The radius of the cylinder is given by r and axis of the cylinder in z -direction. The center-to-center distance between cylinders is given by a . The parameters are chosen with $a \geq 3r$, such that the cylinders are not too close to each other. For frequencies near the dipole resonance, we take the dipole approximation, in which each cylinder is treated as a point dipole[5]. We are interested in the fields perpendicular to the axis of the cylinder in the xy -plane. A magnetic dipole moment $\mathbf{m}(\boldsymbol{\rho}) = \boldsymbol{\alpha}(\omega)\mathbf{B}(\boldsymbol{\rho})$ will be induced when the cylinder at $\boldsymbol{\rho}$ is in a magnetic field $\mathbf{B}(\boldsymbol{\rho})$, where $\boldsymbol{\alpha}(\omega)$ is the polarizability of the cylinder.

We have

$$\boldsymbol{\alpha}(\omega) = \begin{pmatrix} \alpha_{xx} & \alpha_{xy} \\ \alpha_{yx} & \alpha_{yy} \end{pmatrix}. \quad (2.1)$$

In general, the polarizability of an object depends on materials and the geometry of it. We have taken into account the dispersive properties of the materials, so $\boldsymbol{\alpha}(\omega)$ is a function of frequency ω . The polarizability is the response function of an object to the electromagnetic field. Then, the resonant frequency of a single gyromagnetic cylinder ω_0 can be found by solving $\Re[\det \boldsymbol{\alpha}^{-1}(\omega_0)] = 0$. ω_0 can be interpreted as the spectral position of the zero-energy state in the SSH model.

The field at $\boldsymbol{\rho}$ due to the induced dipole moment at $\boldsymbol{\rho}'$ is given by $\mathbf{B}(\boldsymbol{\rho}) = 4\pi k_0^2 \mathbf{G}(\boldsymbol{\rho}, \boldsymbol{\rho}') \mathbf{m}(\boldsymbol{\rho}')$ [60], where $\mathbf{G}(\boldsymbol{\rho}, \boldsymbol{\rho}')$ is the 2D Green's tensor.

We have[61]

$$\mathbf{G}(\boldsymbol{\rho}, \boldsymbol{\rho}') = \begin{pmatrix} G_{xx} & G_{xy} \\ G_{yx} & G_{yy} \end{pmatrix}, \quad (2.2)$$

with

$$G_{xx} = \frac{i}{4} \left(\sin^2(\theta) H_0^{(1)}(k_0 R) + \frac{\cos(2\theta)}{k_0 R} \right) H_1^{(1)}(k_0 R), \quad (2.3a)$$

$$G_{xy} = G_{yx} = \frac{i \sin(2\theta)}{4 \cdot 2} H_2^{(1)}(k_0 R), \quad (2.3b)$$

$$G_{yy} = \frac{i}{4} \left(\cos^2(\theta) H_0^{(1)}(k_0 R) - \frac{\cos(2\theta)}{k_0 R} \right) H_1^{(1)}(k_0 R), \quad (2.3c)$$

where $\mathbf{R} := \boldsymbol{\rho}' - \boldsymbol{\rho} = [R \cos(\theta), R \sin(\theta)] = (x - x', y - y')$ is the relative displacement between the source and the observation points, $H_i^{(1)}$ is the Hankel function of the first kind, and $k_0 = \omega/c$ is the wavenumber in the background medium. In quasi-static limit $k_0 \rightarrow 0$, the field varies inversely as the square of the distance $B \sim 1/R^2$ (see Appendix A). For an array of cylinders, the local field at a dipole is given by the sum of the external field and the fields from all the other dipoles. The dipole-dipole interaction between cylinders leads to the following coupled-dipole equations

$$\mathbf{m}(\boldsymbol{\rho}) = \boldsymbol{\alpha}(\omega) \left(4\pi k_0^2 \sum_{\boldsymbol{\rho}' \neq \boldsymbol{\rho}} \mathbf{G}(\boldsymbol{\rho}, \boldsymbol{\rho}') \mathbf{m}(\boldsymbol{\rho}') + \mathbf{B}_0(\boldsymbol{\rho}) \right), \quad (2.4)$$

where the sum includes all the dipole moments except the self-interaction term and $\mathbf{B}_0(\boldsymbol{\rho})$ is the external excitation magnetic field. For example, \mathbf{B}_0 can be the field of a plane wave.

2.2 Coupled-dipole method in three dimensions

In this section, we describe the coupled-dipole method in three dimensions for multiple dispersive particles and in particular, we consider arrays of gyroelectric spheres. In three dimensions, the polarizability of a particle is generally given by

$$\boldsymbol{\alpha}(\omega) = \begin{pmatrix} \alpha_{xx} & \alpha_{xy} & \alpha_{xz} \\ \alpha_{yx} & \alpha_{yy} & \alpha_{yz} \\ \alpha_{zx} & \alpha_{zy} & \alpha_{zz} \end{pmatrix}. \quad (2.5)$$

Then, the resonant frequency of a single particle ω_0 can again be found by solving $\Re[\det \boldsymbol{\alpha}^{-1}(\omega_0)] = 0$. The field at \mathbf{r} due to the induced dipole moment at \mathbf{r}' is given by $\mathbf{E}(\mathbf{r}) = k_0^2/\epsilon_0 \mathbf{G}(\mathbf{r}, \mathbf{r}') \mathbf{m}(\mathbf{r}')$ [60], where $\mathbf{G}(\mathbf{r}, \mathbf{r}')$ is the 3D Green's tensor. The 3D Green's tensor is obtained from the Helmholtz equation. We have

$$G(\mathbf{r}, \mathbf{r}') = \frac{e^{ik_0 R}}{4\pi R}, \quad (2.6)$$

and

$$\mathbf{G}(\mathbf{r}, \mathbf{r}') = \left(\mathbf{I} + \frac{1}{k_0^2} \nabla \nabla \right) G(\mathbf{r}, \mathbf{r}') \quad (2.7)$$

Then the 3D Green's tensor is given by

$$\mathbf{G}(\mathbf{r}, \mathbf{r}') = \frac{e^{ik_0 R}}{4\pi R} \left[\left(1 + \frac{ik_0 R - 1}{k_0^2 R^2} \right) \mathbf{I} + \frac{3 - 3ik_0 R - k_0^2 R^2}{k_0^2 R^2} \frac{\mathbf{R} \otimes \mathbf{R}}{R^2} \right] \quad (2.8)$$

In quasi-static limit $k_0 \rightarrow 0$, the field varies inversely as $E \sim 1/R^3$ which decays faster than that in two-dimensional space. For an array of sphere, the local field at a dipole is given by the sum of the external field and the fields from all the other dipoles. The dipole-dipole interaction between cylinders leads to the following coupled-dipole equations

$$\mathbf{p}(\mathbf{r}) = \alpha(\omega) \left(\frac{k_0^2}{\epsilon_0} \sum_{\mathbf{r}' \neq \mathbf{r}} \mathbf{G}(\mathbf{r}, \mathbf{r}') \mathbf{m}(\mathbf{r}') + \mathbf{E}_0(\mathbf{r}) \right), \quad (2.9)$$

where the sum includes all the dipole moments except the self-interaction term and $\mathbf{E}_0(\mathbf{r})$ is the external excitation electric field.

2.3 Lattice sums for the 3D Green's tensor

In this section, we describe a method to obtain the lattice sums for the 3D Green's tensor[62]. The lattice sums of the 3D Green's tensor is not diverging but slowly converging. In the study of different photonic systems made of arrays of electromagnetic particles, we often encounter the problem of slowly converging lattice sums. In particular, we follow the method known as Ewald summation and formulate the lattice sums for general 3D Bravais lattices. To begin with, we write the coupled dipole equations as

$$\mathbf{p}(\mathbf{r}) = \alpha(\omega) \left(\frac{k_0^2}{\epsilon_0} \sum_{n \neq 0} \mathbf{G}(\mathbf{R}_0, \mathbf{R}_0 + \mathbf{R}_n) \mathbf{p}(\mathbf{R}_0 + \mathbf{R}_n) + \mathbf{E}_0(\mathbf{R}_0) \right), \quad (2.10)$$

where the Bravais lattice vector is given by

$$\mathbf{R}_n = n_1 \mathbf{a}_1 + n_2 \mathbf{a}_2 + n_3 \mathbf{a}_3 \quad (2.11)$$

and we define $\mathbf{R} := \mathbf{r} - \mathbf{r}'$ and the reference point $\mathbf{R}_0 = n_{1,0} \mathbf{a}_1 + n_{2,0} \mathbf{a}_2 + n_{3,0} \mathbf{a}_3$. For infinite periodic lattice, we apply the Bloch's theorem

$$\mathbf{p}(\mathbf{R}_0 + \mathbf{R}_n) = e^{i\mathbf{k} \cdot \mathbf{R}_n} \mathbf{p}(\mathbf{R}_0) \quad (2.12)$$

where $\mathbf{k} = k_x \mathbf{x} + k_y \mathbf{y} + k_z \mathbf{z}$ is the Bloch's wave vector. Then the coupled-dipole equation for infinite lattice is given by

$$\mathbf{p}(\mathbf{r}) = \alpha(\omega) \left(\frac{k_0^2}{\epsilon_0} \sum_{n \neq 0} \mathbf{G}(\mathbf{R}_0, \mathbf{R}_0 + \mathbf{R}_n) e^{i\mathbf{k} \cdot \mathbf{R}_n} \mathbf{p}(\mathbf{R}_0) + \mathbf{E}_0(\mathbf{R}_0) \right) \quad (2.13)$$

The lattice sums is given by $\sum_{n \neq 0} \mathbf{G}(\mathbf{r}, \mathbf{R}_0 + \mathbf{R}_n) e^{i\mathbf{k} \cdot \mathbf{R}_n}$, where we now consider the observation point in general position \mathbf{r} other than only the lattice point. First, we observed that there is singularity at $\mathbf{r} = \mathbf{R}_0$ with $n = 0$. To carry out regularization, we rewrite the lattice Green's function as

$$\mathbf{G}(\mathbf{r}, \mathbf{R}_0 + \mathbf{R}_n, \mathbf{k}) = \sum_{n=-\infty}^{\infty} \mathbf{G}(\mathbf{r}, \mathbf{R}_0 + \mathbf{R}_n) e^{i\mathbf{k} \cdot \mathbf{R}_n} - \mathbf{G}(\mathbf{r}, \mathbf{R}_0) \quad (2.14)$$

$$\mathbf{G}(\mathbf{R}_0, \mathbf{R}_0 + \mathbf{R}_n, \mathbf{k}) = \lim_{\mathbf{r} \rightarrow \mathbf{R}_0} \left(\sum_{n=-\infty}^{\infty} \mathbf{G}(\mathbf{r}, \mathbf{R}_0 + \mathbf{R}_n) e^{i\mathbf{k} \cdot \mathbf{R}_n} - \mathbf{G}(\mathbf{r}, \mathbf{R}_0) \right) \quad (2.15)$$

The Green's tensor is related to the Green's function by

$$\mathbf{G}(\mathbf{r}, \mathbf{R}_0 + \mathbf{R}_n, \mathbf{k}) = \left(\mathbf{I} + \frac{1}{k_0^2} \nabla \nabla \right) \sum_{n=-\infty}^{\infty} \mathbf{G}(r, \mathbf{R}_0 + \mathbf{R}_n) e^{i\mathbf{k} \cdot \mathbf{R}_n} - \mathbf{G}(r, \mathbf{R}_0) \quad (2.16)$$

and

$$\mathbf{G}(\mathbf{R}_0, \mathbf{R}_0 + \mathbf{R}_n, \mathbf{k}) = \lim_{r \rightarrow \mathbf{R}_0} \mathbf{G}(r, \mathbf{R}_0 + \mathbf{R}_n, \mathbf{k}) \quad (2.17)$$

Following the Ewald method, then we can carry out the sums in the real space lattice and reciprocal space lattice respectively, which gives

$$\mathbf{G}(\mathbf{R}_0, \mathbf{R}_0 + \mathbf{R}_n, \mathbf{k}) = \mathbf{G}_R + \mathbf{G}_G \quad (2.18)$$

and

$$G\mathbf{R}_0, \mathbf{R}_0 + \mathbf{R}_n, \mathbf{k}) = G_R + G_G \quad (2.19)$$

To be clear, the reciprocal lattice is given by

$$\mathbf{G}_m = m_1 \mathbf{b}_1 + m_2 \mathbf{b}_2 + m_3 \mathbf{b}_3 \quad (2.20)$$

where

$$\mathbf{b}_1 = 2\pi \frac{\mathbf{a}_2 \times \mathbf{a}_3}{\mathbf{a}_1 \cdot (\mathbf{a}_2 \times \mathbf{a}_3)} \quad (2.21)$$

$$\mathbf{b}_2 = 2\pi \frac{\mathbf{a}_3 \times \mathbf{a}_1}{\mathbf{a}_2 \cdot (\mathbf{a}_3 \times \mathbf{a}_1)} \quad (2.22)$$

$$\mathbf{b}_3 = 2\pi \frac{\mathbf{a}_1 \times \mathbf{a}_2}{\mathbf{a}_3 \cdot (\mathbf{a}_1 \times \mathbf{a}_2)} \quad (2.23)$$

To simplify the notation, we further define

$$\mathbf{r}_n = \mathbf{r} - (\mathbf{R}_0 + \mathbf{R}_n) \quad (2.24)$$

and hence

$$r_n = \mathbf{r} - |(\mathbf{R}_0 + \mathbf{R}_n)| \quad (2.25)$$

Then we have

$$G_R = \frac{1}{8\pi} \sum_{n=-\infty}^{\infty} \frac{e^{i\mathbf{k} \cdot \mathbf{R}_n}}{r_n} f(r_n) \quad (2.26)$$

and

$$G_G = \frac{1}{a_1 a_2 a_3} \sum_{m=-\infty}^{\infty} \frac{e^{-\frac{|\mathbf{k} + \mathbf{G}_m|^2 - k_0^2}{4E^2}}}{|\mathbf{k} + \mathbf{G}_m|^2 - k_0^2} e^{i(\mathbf{k} + \mathbf{G}_m) \cdot (\mathbf{r} - \mathbf{R}_0)} \quad (2.27)$$

where we define the function

$$f(\mathbf{r}, \mathbf{R}_0 + \mathbf{R}_n) := e^{ik_0|\mathbf{r} - (\mathbf{R}_0 + \mathbf{R}_n)|} \operatorname{erfc}(|\mathbf{r} - (\mathbf{R}_0 + \mathbf{R}_n)|E + \frac{ik_0}{2E}) \quad (2.28)$$

$$+ e^{-ik_0|\mathbf{r} - (\mathbf{R}_0 + \mathbf{R}_n)|} \operatorname{erfc}(|\mathbf{r} - (\mathbf{R}_0 + \mathbf{R}_n)|E - \frac{ik_0}{2E}) \quad (2.29)$$

$$f(r_n) = e^{ik_0 r_n} \operatorname{erfc}(r_n E + \frac{ik_0}{2E}) + e^{-ik_0 r_n} \operatorname{erfc}(r_n E - \frac{ik_0}{2E}) \quad (2.30)$$

The parameter E is chosen to optimized the convergence and it is given by

$$E = \left(\pi^2 \frac{1/a_1^2 + 1/a_2^2 + 1/a_3^2}{a_1^2 + a_2^2 + a_3^2} \right)^{1/4} \quad (2.31)$$

Now, we can carry out the differentiation to G_R and G_G respectively. For

the real lattice part, we have

$$\nabla\nabla G_R = \frac{1}{8\pi} \sum_{n=-\infty}^{\infty} e^{i\mathbf{k}\cdot\mathbf{R}_n} \mathbf{F}(r_n) \quad (2.32)$$

where

$$\mathbf{F}(r_n) := \left(\frac{f'(r_n)}{r_n^2} - \frac{f(r_n)}{r_n^3} \right) \mathbf{I} + \left(\frac{f''(r_n)}{r_n} - \frac{3f'(r_n)}{r_n^2} + \frac{3f(r_n)}{r_n^3} \right) \frac{\mathbf{r}_n \otimes \mathbf{r}_n}{r_n^2} \quad (2.33)$$

For the reciprocal lattice part, we have

$$\nabla\nabla G_G = -\frac{1}{a_1 a_2 a_3} \sum_{m=-\infty}^{\infty} (\mathbf{k} + \mathbf{G}_m) \otimes (\mathbf{k} + \mathbf{G}_m) \frac{e^{-\frac{|\mathbf{k} + \mathbf{G}_m|^2 - k_0^2}{4E^2}}}{|\mathbf{k} + \mathbf{G}_m|^2 - k_0^2} e^{i(\mathbf{k} + \mathbf{G}_m) \cdot (\mathbf{r} - \mathbf{R}_0)} \quad (2.34)$$

From these, we already obtained the field from a infinite lattice to an arbitrary observation point \mathbf{r} . In the study of the properties of an infinite lattice, we will need the observation point to be one of the lattice point. For $\mathbf{r} = \mathbf{R}_0$, it is done by regularizing the Green's function to remove the singularity

$$G(\mathbf{R}_0, \mathbf{R}_0 + \mathbf{R}_n, \mathbf{k}) = \lim_{\mathbf{r} \rightarrow \mathbf{R}_0} (G_R(\mathbf{r}, \mathbf{R}_0 + \mathbf{R}_n, \mathbf{k}) - G(\mathbf{r}, \mathbf{R}_0)) \quad (2.35)$$

$$G(\mathbf{R}_0, \mathbf{R}_0 + \mathbf{R}_n, \mathbf{k}) = \frac{1}{8\pi} \left(\sum_{n \neq 0} \frac{e^{i\mathbf{k}\cdot\mathbf{R}_n}}{r_n} f(r_n) + f'(0) - 2ik_0 \right) \quad (2.36)$$

$$G_G(\mathbf{R}_0) = \frac{1}{a_1 a_2 a_3} \sum_{m=-\infty}^{\infty} \frac{e^{-\frac{|\mathbf{k} + \mathbf{G}_m|^2 - k_0^2}{4E^2}}}{|\mathbf{k} + \mathbf{G}_m|^2 - k_0^2} \quad (2.37)$$

Then we can carry out differentiation on the real lattice part and reciprocal

lattice part respectively.

$$\nabla\nabla G(\mathbf{R}_0, \mathbf{R}_0 + \mathbf{R}_n, \mathbf{k}) = \lim_{r \rightarrow \mathbf{R}_0} (\nabla\nabla G_R(r, \mathbf{R}_0 + \mathbf{R}_n, \mathbf{k}) - \nabla\nabla G(r, \mathbf{R}_0)) \quad (2.38)$$

$$\nabla\nabla G(\mathbf{R}_0, \mathbf{R}_0 + \mathbf{R}_n, \mathbf{k}) = \frac{1}{8\pi} \left(\sum_{n \neq 0} \frac{e^{i\mathbf{k} \cdot \mathbf{R}_n}}{r_n} f(r_n) + \frac{f'''(0) + 2ik_0^3}{3} \mathbf{I} \right) \quad (2.39)$$

$$\nabla\nabla G_G(\mathbf{R}_0) = -\frac{1}{a_1 a_2 a_3} \sum_{m=-\infty}^{\infty} (\mathbf{k} + \mathbf{G}_m) \otimes (\mathbf{k} + \mathbf{G}_m) \frac{e^{-\frac{|\mathbf{k} + \mathbf{G}_m|^2 - k_0^2}{4E^2}}}{|\mathbf{k} + \mathbf{G}_m|^2 - k_0^2} \quad (2.40)$$

2.4 Eigen-response theory

Instead of solving Eq. (2.9) directly, which involves numerical complex root-finding, we use an eigen-response theory to study the spectral response of the system. To do so, we define

$$\mathbf{M}(\omega) := \boldsymbol{\alpha}^{-1}(\omega) - 4\pi k_0^2 \sum_{\rho' \neq \rho} \mathbf{G}(\rho, \rho'). \quad (2.41)$$

For a system with N gyromagnetic cylinders, $\mathbf{M}(\omega)$ is a $2N \times 2N$ matrix. Then Eq. (2.9) can be rewritten as

$$\mathbf{M}(\omega) \mathbf{m} = \mathbf{B}_0. \quad (2.42)$$

This relates the dipole moments \mathbf{m} with the external excitation field \mathbf{B}_0 . In the eigen-response theory [57, 58, 4, 59], which is based on spectral decompo-

sition, we consider the eigenvalue problem

$$\mathbf{M}(\omega)\mathbf{m}_i = \lambda_i(\omega)\mathbf{m}_i, \quad (2.43)$$

where $\lambda_i(\omega)$ is the eigenvalue corresponding to the eigenmode \mathbf{m}_i . We define the quantity

$$\alpha_{\text{eig}} := \frac{1}{\lambda}, \quad (2.44)$$

as the eigen-polarizability, which has the dimension cm^2 , same as that of the polarizability α . The eigen-polarizability can be interpreted as the response function of the corresponding eigenmode for an external excitation field and the peaks of $\Im(\alpha_{\text{eig}})$ represent resonances.

2.5 Zak phase and bulk-boundary correspondence

To classify the band topology in 1D systems, we consider a 1D infinite lattice with the wave vector $\mathbf{k} = k\hat{\mathbf{x}}$, with the first Brillouin zone $k \in [-\pi/a, \pi/a]$, where a is the lattice constant. The topological invariant for 1D system is given by Zak phase[63], which is the 1D Berry phase. For the SSH model, which is a two-band model, we have the eigenmode $\mathbf{m}_{\pm}(k)$ for each band (+ or -), which is a function of the wave vector k . The Zak phase for each band

is given by[40]

$$\theta_{\pm} = i \int_{-\pi/a}^{\pi/a} \mathbf{m}_{\pm}^*(k) \cdot \frac{d}{dk} \mathbf{m}_{\pm}(k) dk, \quad (2.45)$$

We can calculate the Zak phase numerically through the Wilson loop

$$e^{-i\theta_{\pm}} = \prod_0^{N-1} \frac{\mathbf{m}_{\pm}^*(-\pi + n\Delta k) \mathbf{m}_{\pm}(-\pi + (n+1)\Delta k)}{|\mathbf{m}_{\pm}^*(-\pi + n\Delta k) \mathbf{m}_{\pm}(-\pi + (n+1)\Delta k)|}, \quad (2.46)$$

where $\Delta k = 2\pi/N$ with N the number of unit cell. In the continuum limit, we have $N \rightarrow \infty$ and $\Delta k \rightarrow 0$, then Eq. (2.46) becomes Eq. (2.45). The Zak phase for system with unit cell having inversion symmetry is a Z_2 invariant and quantized to 0 and π

$$\theta_{\pm} = n\pi \pmod{2\pi} \quad (2.47)$$

If the inversion center of the unit cell is not at the center of it, the Zak phase is not quantized, but can be recovered by an additional term[64, 65]. For the SSH model, this problem will not occur and Eq. (2.45) always gives quantized Zak phase.

The Zak phase for each bands is obtained from the bulk Hamiltonian. This bulk topological invariant can be used to make simple robust predictions about the physics at the edge of a finite lattice. The number of edge modes n_{edge} in the gap of a finite lattice is given by[56, 65]

$$n_{\text{edge}} = \frac{\theta}{\pi} \pmod{2} \quad (2.48)$$

This is known as the bulk-boundary correspondence.

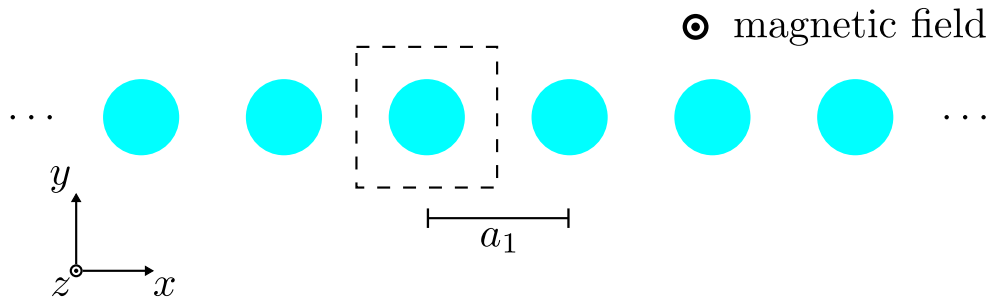


Figure 3.1: Illustration of gyromagnetic cylinders on 1D infinite lattice. The lattice constant is given by a_1 . The unit cell is indicated by the dashed box.

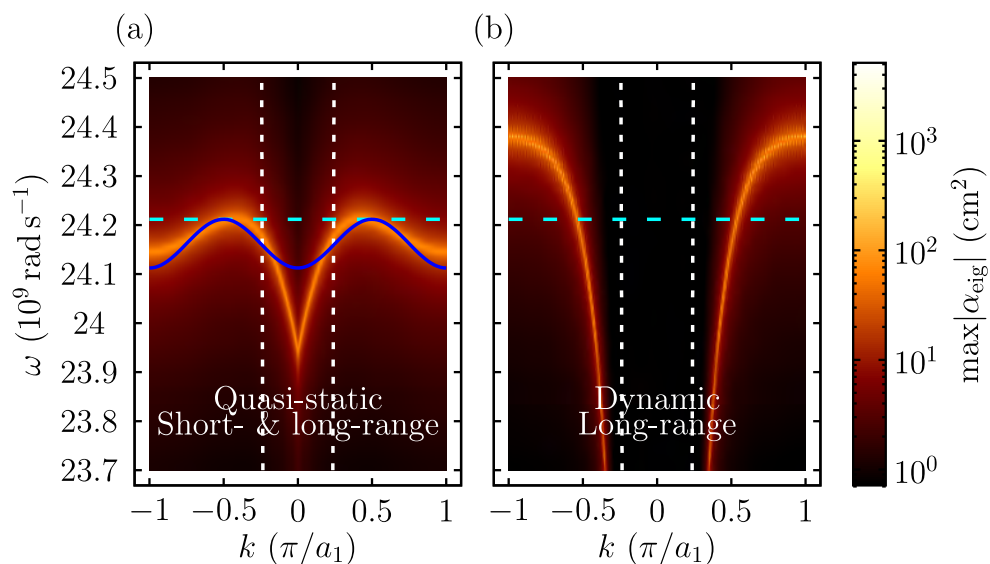


Figure 3.2: (a) The photonic band structure with short- and long-range interactions in quasi-static limit. The blue line is the dispersion relation with nearest-neighbor interactions only. (b) The photonic band structure with dynamic long-range interactions. The white dotted lines are the light lines and the region within the light lines is the light cone. The cyan dashed line indicates the resonant frequency of a single gyromagnetic cylinder ω_0 .

Chapter 3

One-dimensional (1D) gyromagnetic lattices

3.1 Regular chain

3.1.1 Infinite lattice

We begin by considering a 1D infinite lattice with lattice constant $a_1 = 9.375$ mm in x -direction as depicted in Fig. 3.1. The unit cell consists of one gyromagnetic cylinder with radius $r = 2.5$ mm and axis of the cylinder in z -direction. The parameters are chosen with $a_1 \geq 3r$, such that the cylinders are not too close to each other. For frequencies near the dipole resonance, we take the dipole approximation, in which each cylinder is treated as a point dipole[5]. We are interested in the fields of the dipole moments in the xy -

plane, which are perpendicular to the axis of the cylinder. The polarizability of a cylinder is given by[66]

$$\boldsymbol{\alpha}^{-1}(\omega) = \frac{4\pi}{A} ([\boldsymbol{\mu}(\omega) - \mathbf{I}]^{-1} + \mathbf{L}) - i\frac{\pi k_0^2}{2}\mathbf{I}, \quad (3.1)$$

where $A = \pi r^2$, \mathbf{I} is the 2×2 identity matrix, and $\mathbf{L} = (1/2)\mathbf{I}$ is the demagnetization factors for cylinder, $k_0 = \omega/c$ is the wavenumber in the background medium and $\boldsymbol{\mu}(\omega)$ is the permeability tensor of the gyromagnetic medium. The radiative correction term $-i(\pi k_0^2/2)\mathbf{I}$ is included to satisfy the optical theorem. For the case that the applied static magnetic field \mathbf{H} and the saturation magnetization \mathbf{M} are parallel to the axis of the cylinder in $+z$ -direction, the permeability tensor is given by[67]

$$\boldsymbol{\mu}(\omega) = \begin{pmatrix} \mu_1 & -i\mu_2 \\ i\mu_2 & \mu_1 \end{pmatrix}, \quad (3.2)$$

with

$$\mu_1 = 1 + \frac{\omega_m(\omega_h - i\beta\omega)}{(\omega_h - i\beta\omega)^2 - \omega^2}, \quad (3.3a)$$

$$\mu_2 = \frac{\omega_m\omega}{(\omega_h - i\beta\omega)^2 - \omega^2}, \quad (3.3b)$$

where $\omega_h = \gamma H$ and $\omega_m = \gamma 4\pi M$, in which γ is the gyromagnetic ratio, and β is the damping factor. We consider the cylinders are made of yttrium iron garnet (YIG), which is a ferrimagnetic material with very low

loss. The parameters for YIG are $H = 500$ Oe, $4\pi M = 1750$ G[51, 53], and $\beta = 3 \times 10^{-4}$ [68]. From these expressions, we have

$$\boldsymbol{\alpha}^{-1}(\omega) = \begin{pmatrix} \frac{4}{r^2} \left(\frac{\omega_h}{\omega_m} + \frac{1}{2} - i\beta \frac{\omega}{\omega_m} \right) - i \frac{\pi k_0^2}{2} & i \frac{4}{r^2} \left(\frac{\omega}{\omega_m} \right) \\ -i \frac{4}{r^2} \left(\frac{\omega}{\omega_m} \right) & \frac{4}{r^2} \left(\frac{\omega_h}{\omega_m} + \frac{1}{2} - i\beta \frac{\omega}{\omega_m} \right) - i \frac{\pi k_0^2}{2} \end{pmatrix}. \quad (3.4)$$

The resonant frequency of a single gyromagnetic cylinder ω_0 is found by solving $\Re[\det \boldsymbol{\alpha}^{-1}(\omega_0)] = 0$, which gives

$$\omega_0 = \omega_h + \frac{\omega_m}{2}. \quad (3.5)$$

It is equal to $f_0 = \omega_0/(2\pi) = 3.853$ GHz, which is in the microwave regime. ω_0 can be interpreted as the spectral position of the zero-energy state in the SSH model.

For our system, we have the 2D Green's tensor[61]

$$\mathbf{G}(\boldsymbol{\rho}, \boldsymbol{\rho}') = \begin{pmatrix} G_{xx} & 0 \\ 0 & G_{yy} \end{pmatrix}, \quad (3.6)$$

with

$$G_{xx} = \frac{i}{4} \left(\frac{1}{k_0 R} \right) H_1^{(1)}(k_0 R), \quad (3.7a)$$

$$G_{yy} = \frac{i}{4} \left(H_0^{(1)}(k_0 R) - \frac{1}{k_0 R} H_1^{(1)}(k_0 R) \right), \quad (3.7b)$$

where $\mathbf{R} := \boldsymbol{\rho}' - \boldsymbol{\rho}$ is the relative displacement between the source and the observation points, and $H_i^{(1)}$ is the Hankel function of the first kind. We have the following coupled-dipole equations

$$\mathbf{m}(\boldsymbol{\rho}) = \boldsymbol{\alpha}(\omega) \left(4\pi k_0^2 \sum_{\boldsymbol{\rho}' \neq \boldsymbol{\rho}} \mathbf{G}(\boldsymbol{\rho}, \boldsymbol{\rho}') \mathbf{m}(\boldsymbol{\rho}') + \mathbf{B}_0(\boldsymbol{\rho}) \right), \quad (3.8)$$

where the sum includes all the dipole moments except the self-interaction term and $\mathbf{B}_0(\boldsymbol{\rho})$ is the external excitation magnetic field.

For 1D infinite lattice, the translational symmetry leads to Bloch's theorem

$$\mathbf{m}(\boldsymbol{\rho} + \mathbf{R}) = e^{i\mathbf{k} \cdot \mathbf{R}} \mathbf{m}(\boldsymbol{\rho}), \quad (3.9)$$

where the displacement $\mathbf{R} = na_1 \hat{\mathbf{x}}$, with integer n and lattice constant a_1 , and the wave vector $\mathbf{k} = k \hat{\mathbf{x}}$, with the first Brillouin zone $k \in [-\pi/a_1, \pi/a_1]$. Also, we have $\mathbf{G}(\boldsymbol{\rho}, \boldsymbol{\rho}') = \mathbf{G}(0, \mathbf{R})$. The coupled-dipole equation for infinite lattice is given by

$$\mathbf{m}(\boldsymbol{\rho}) = \boldsymbol{\alpha}(\omega) \left(4\pi k_0^2 \sum_{\mathbf{R} \neq 0} \mathbf{G}(0, \mathbf{R}) e^{i\mathbf{k} \cdot \mathbf{R}} \mathbf{m}(\boldsymbol{\rho}) + \mathbf{B}_0(\boldsymbol{\rho}) \right), \quad (3.10)$$

and we define

$$\mathbf{M}(\mathbf{k}, \omega) := \boldsymbol{\alpha}^{-1}(\omega) - 4\pi k_0^2 \sum_{\mathbf{R} \neq 0} \mathbf{G}(0, \mathbf{R}) e^{i\mathbf{k} \cdot \mathbf{R}}. \quad (3.11)$$

The translational symmetry reduces \mathbf{M} to a 2×2 matrix. Then Eq. (3.10)

can be rewritten as

$$\mathbf{M}(\mathbf{k}, \omega)\mathbf{m} = \mathbf{B}_0. \quad (3.12)$$

Then the eigenvalue problem for infinite lattice is

$$\mathbf{M}(\mathbf{k}, \omega)\mathbf{m}_i = \lambda_i(\mathbf{k}, \omega)\mathbf{m}_i. \quad (3.13)$$

It should be noted that, \mathbf{M} is non-Hermitian due to the loss and dynamic effects. From now on, we set $\mathbf{B}_0 = 0$, so as to study the normal modes of the system.

Quasi-static limit

We calculate the band structure of the gyromagnetic system described in Sec. 3.1.1 in an infinite lattice. Before studying the more general case, we consider the system in quasi-static limit $k_0 \rightarrow 0$. The coupled-dipole equations in quasi-static limit is described in Appendix A. From Eq. (A.10), we have

$$\mathbf{M}'(\mathbf{k}, \omega) = \begin{pmatrix} \frac{4}{r^2} \left(\frac{\omega_h}{\omega_m} + \frac{1}{2} - i\beta \frac{\omega}{\omega_m} \right) - \sum_{\mathbf{R} \neq 0} \frac{2}{R^2} e^{i\mathbf{k} \cdot \mathbf{R}} & i \frac{4}{r^2} \left(\frac{\omega}{\omega_m} \right) \\ -i \frac{4}{r^2} \left(\frac{\omega}{\omega_m} \right) & \frac{4}{r^2} \left(\frac{\omega_h}{\omega_m} + \frac{1}{2} - i\beta \frac{\omega}{\omega_m} \right) + \sum_{\mathbf{R} \neq 0} \frac{2}{R^2} e^{i\mathbf{k} \cdot \mathbf{R}} \end{pmatrix}. \quad (3.14)$$

Then, the system is described by

$$\mathbf{M}'(\mathbf{k}, \omega)\mathbf{m} = 0. \quad (3.15)$$

Now, we take the tight-binding approach, in which only short-range interactions are being considered. By including only the nearest-neighbor interactions, the dispersion relation and the normal mode can be obtained analytically by solving the non-trivial solution of Eq. (3.15). From $\Re[\det \mathbf{M}'(\mathbf{k}, \omega)] = 0$, we obtain the dispersion relation

$$\omega(k) = \omega_0 \sqrt{1 - f(k)^2}, \quad (3.16)$$

with

$$f(k) := \left(\frac{r}{a_1} \right)^2 \frac{\omega_m}{\omega_0} \cos(ka_1). \quad (3.17)$$

It is plotted with blue line in Fig. 3.2 (a). We observe a single narrowband. The normal mode of the system does not couple to the photon mode of the background medium. At $k = \pm\pi/(2a_1)$, the resonant frequency of the system equals to that of a single gyromagnetic cylinder ω_0 , while at other k , the band is below ω_0 . The group velocity $v_g = d\omega/dk$ of the normal mode is zero, $v_g = 0$, at $k = 0, \pm\pi/(2a_1), \pm\pi/a_1$. We will soon show that the results obtained in quasi-static limit do not correctly describe the qualitative features of the system. Nevertheless, we see that only one non-trivial solution is obtained from the 2×2 matrix problem of Eq. (3.15). The normalized normal mode is given by

$$\mathbf{m} = \frac{1}{\sqrt{2}} \begin{pmatrix} \sqrt{1 + f(k)} e^{-i\frac{\pi}{2}} \\ \sqrt{1 - f(k)} \end{pmatrix}. \quad (3.18)$$

We find that the longitudinal mode and the transverse mode are coupled, such that the magnetic dipole moments rotate counterclockwise elliptically. This is different from the analogous plasmonic system, where two non-trivial solutions, which correspond to the longitudinal mode and the transverse mode, will be obtained.

Dynamic long-range interaction

Now, we extend our calculation to include the dynamic long-range interactions. We consider the non-Hermitian eigenvalue problem of Eq. (3.13) with eigen-response theory. The band structure can be obtained from the peaks of $\max|\alpha_{\text{eig}}|$ and it is shown in Fig. 3.2 (b). Different from the result calculated with quasi-static short-range interactions, we observe a single broadband. The normal modes of the system coupled strongly to the photon mode of the background medium. The band forms outside the light cone with $|k| > \omega/c$, which represent guided modes and any mode in the light cone with $|k| < \omega/c$ is radiation mode[69]. There is blueshift near the Brillouin zone boundary, such that the band is above the resonant frequency of a single gyromagnetic cylinder ω_0 . All of these features are different from the results in quasi-static limit.

To show that the differences are due to the dynamic effects, we consider the system in quasi-static limit again, but including long-range interactions.

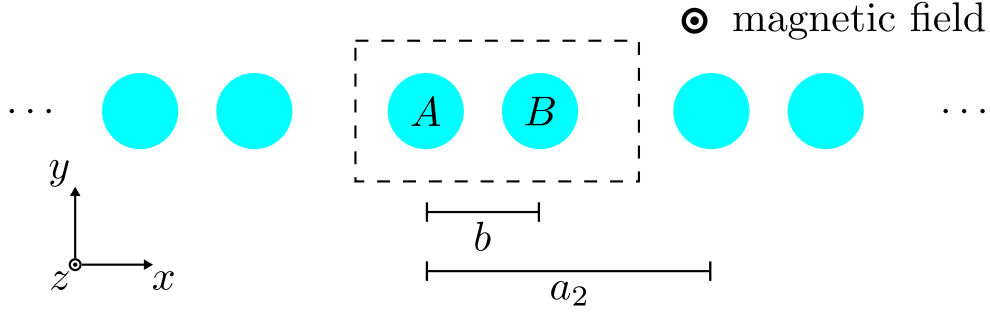


Figure 3.3: Illustration of dimer model of gyromagnetic cylinders on 1D infinite lattice. The lattice constant is given by a_2 . The unit cell is indicated by the dashed box. The distance between cylinder A and cylinder B is given by $b = (1 - \delta)a_2/2$.

Now, we have the eigenvalue problem

$$\mathbf{M}'(\mathbf{k}, \omega) \mathbf{m}_i = \lambda_i(\mathbf{k}, \omega) \mathbf{m}_i, \quad (3.19)$$

where $\mathbf{M}'(\mathbf{k}, \omega)$ is given by Eq. (3.14). The band structure is shown in Fig. 3.2 (a). We see that, without the dynamic effects, the general features of the band are similar to the blue line, which is the dispersion relation obtained with only short-range interactions, except at the Brillouin zone center $k = 0$, where the group velocity v_g becomes discontinuous.

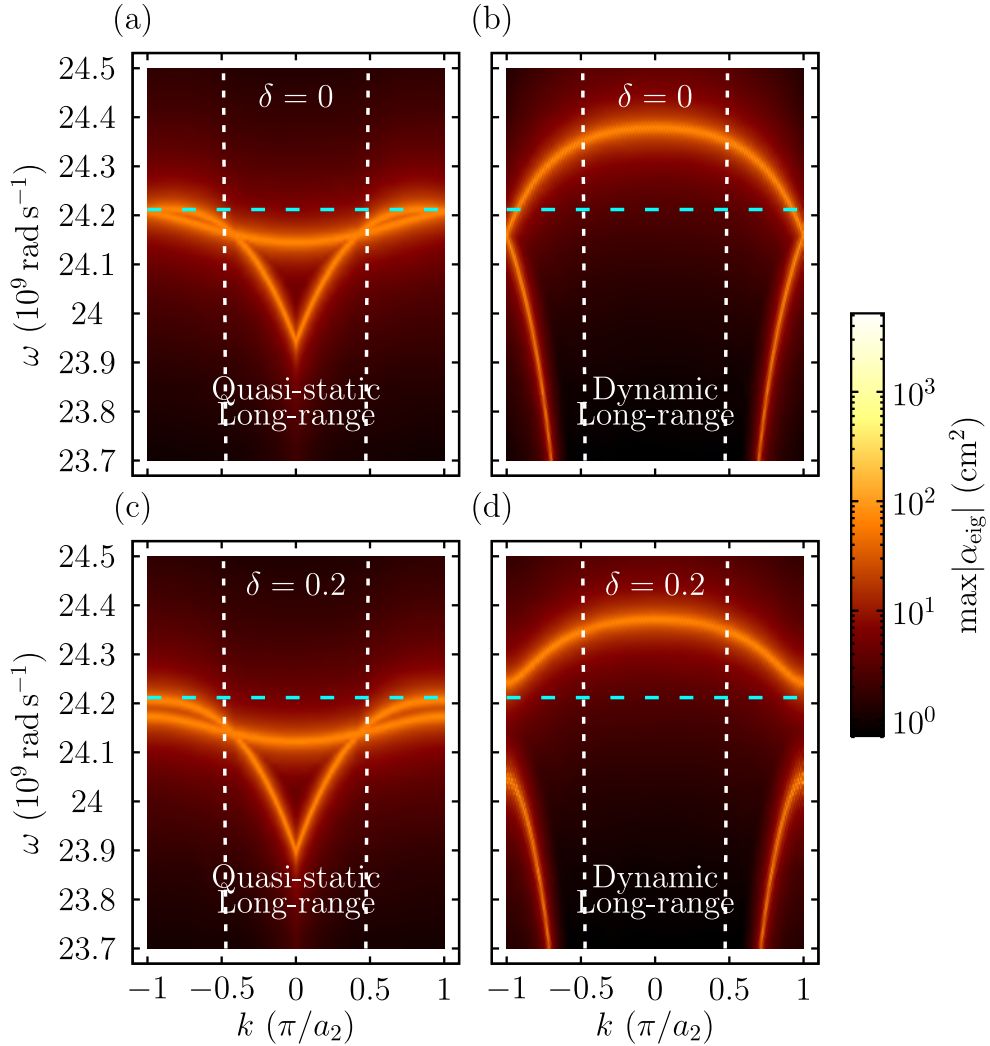


Figure 3.4: (a), (b), (c), (d) The photonic band structure for dimer model in quasi-static limit and in general, with dynamic effects. All results include the long-range interactions. The white dotted lines are the light lines and the region within the light lines is the light cone. The cyan dashed line indicates the resonant frequency of a single gyromagnetic cylinder ω_0 .

3.2 Dimerized chain

3.2.1 Model

To further demonstrate the importance of dynamic long-range interactions in gyromagnetic systems, we consider a dimer model of gyromagnetic cylinders on 1D infinite lattices. In this dimer model, the lattice constant is given by $a_2 = 2a_1 = 18.75$ mm. The unit cell consists of two gyromagnetic cylinders, labeled as A and B , with the same radius $r = 2.5$ mm. The displacement from cylinder A to cylinder B is given by $\mathbf{b} = b\hat{\mathbf{x}}$, with

$$b = \frac{a_2}{2}(1 - \delta), \quad (3.20)$$

where δ is a dimensionless parameter with $|\delta| \leq 0.2$ and hence $b \geq 3r$. The system is depicted in Fig. 3.3. The polarizability for cylinder A and cylinder B are given by $\boldsymbol{\alpha}_A$ and $\boldsymbol{\alpha}_B$, and their corresponding magnetic dipole moments are given by \mathbf{m}_A and \mathbf{m}_B , respectively. With Bloch's theorem in Eq. (3.9), the coupled-dipole equations for the dimer model can be written as

$$\begin{pmatrix} \boldsymbol{\alpha}_A^{-1} & 0 \\ 0 & \boldsymbol{\alpha}_B^{-1} \end{pmatrix} \begin{pmatrix} \mathbf{m}_A \\ \mathbf{m}_B \end{pmatrix} = \boldsymbol{\Gamma} \begin{pmatrix} \mathbf{m}_A \\ \mathbf{m}_B \end{pmatrix}, \quad (3.21)$$

with

$$\Gamma := 4\pi k_0^2 \begin{pmatrix} \sum_{\mathbf{R} \neq 0} \mathbf{G}(0, \mathbf{R}) e^{i\mathbf{k} \cdot \mathbf{R}} & \sum_{\mathbf{R}} \mathbf{G}(0, \mathbf{R} + \mathbf{b}) e^{i\mathbf{k} \cdot \mathbf{R}} \\ \sum_{\mathbf{R}} \mathbf{G}(0, \mathbf{R} - \mathbf{b}) e^{i\mathbf{k} \cdot \mathbf{R}} & \sum_{\mathbf{R} \neq 0} \mathbf{G}(0, \mathbf{R}) e^{i\mathbf{k} \cdot \mathbf{R}} \end{pmatrix}, \quad (3.22)$$

and the associated eigenvalue problem with eigen-response theory is given by

$$\mathbf{M}_{\text{dimer}}(\mathbf{k}, \omega) \mathbf{m}_i = \lambda_i(\mathbf{k}, \omega) \mathbf{m}_i, \quad (3.23)$$

where

$$\mathbf{M}_{\text{dimer}}(\mathbf{k}, \omega) := \begin{pmatrix} \boldsymbol{\alpha}_A^{-1} & 0 \\ 0 & \boldsymbol{\alpha}_B^{-1} \end{pmatrix} - \Gamma, \quad (3.24)$$

is a non-Hermitian 4×4 matrix.

We consider the system with $\delta = 0$ and $\delta = 0.2$, in quasi-static limit (see Appendix B) and in general, with dynamic effects, all with long-range interactions. Again, the band structure can be obtained from the peaks of $\max|\alpha_{\text{eig}}|$. For $\delta = 0$, the system is the same as that discussed in Sec. 3.1.1 as depicted in Fig. 3.1. The band structures for this system are shown in Fig. 3.4 (a) and (b). Two bands are obtained due to the band folding and they are physically the same with those in Fig. 3.2 (a) and (b). In both cases, the results are gapless and there is degeneracy at the Brillouin zone boundary $k = \pm\pi/a_2$ protected by the inversion symmetry of the system. For the case in quasi-static limit, this degeneracy is at the resonant frequency of a single gyromagnetic cylinder ω_0 , while for the case with dynamic effects, it is at a

frequency below ω_0 .

For $\delta = 0.2$, the band structures are shown in Fig. 3.4 (c) and (d). Again, two bands are obtained. For any $\delta \neq 0$, the inversion symmetry of the system is broken, hence the degeneracy split. For the case in quasi-static limit, the degeneracy at the Brillouin zone boundary $k = \pm\pi/a_2$ is split by one band shifting to a lower frequency, such that the two bands do not exceed the resonant frequency of a single gyromagnetic cylinder ω_0 . The system does not have a full band gap. While for the case with dynamic effects, the system opens a full band gap. The degeneracy at the Brillouin zone boundary $k = \pm\pi/a_2$ is split, such that the bands are symmetric about the original degeneracy. Moreover, the band gap is larger than the one in quasi-static limit.

We showed that, for dimer model of gyromagnetic cylinders on 1D infinite lattice, the system do not have a full band gap in quasi-static limit, even if long-range interactions are included. Besides breaking inversion symmetry of the system, a full band gap is obtained only when the dynamic long-range interactions are taken into account. This is a major difference with the conventional SSH model and its analogous systems, such as arrays of plasmonic[40, 42] and dielectric nanoparticles[46, 48]. In plasmonic lattices, although dynamic long-range interactions can be also considered[43, 44, 45], studying the system in quasi-static limit, with only short-range interactions is suffice to obtained a full band gap[46, 40, 48, 42], as long as inversion symmetry is broken in the system. Furthermore, chiral symmetry of the

system is broken due to the dynamic long-range interactions[44, 45], such that the band structures are not symmetric with respect to the resonant frequency of a single cylinder ω_0 . These demonstrated the importance of dynamic long-range interactions on the band structures in gyromagnetic systems.

3.2.2 Topological phase transition

It is known that, for the conventional SSH model, the topology of band depends on the distance between the two basis elements in the unit cell[70]. Here, we discuss the topological phase transition in the dimer model of gyromagnetic cylinders on 1D infinite lattices by the associated band inversion[71].

We consider the band structures of the system for $\delta \in [-0.2, 0.2]$ and find the corresponding upper and lower band edges at $k = \pi/a_2$. The results are shown in Fig. 3.5. The curves are the upper and lower band edges at $k = \pi/a_2$ and the grey areas are the band gaps. The results are symmetric about $\delta = 0$. For $\delta \neq 0$, the system opens a band gap. As $|\delta|$ decrease, the band gap becomes smaller. For $\delta = 0$, the band gap closes, and the system is gapless, which corresponds to the results in Fig. 3.4 (b) at $k = \pi/a_2$. To illustrate the band inversion, we find the eigenmodes of the unit cell with $\delta = 0.2$ and $\delta = -0.2$ for both the upper band and the lower band. We see that, all the magnetic dipole moments rotate counterclockwise elliptically, as discussed in Sec. 3.1.1. There are two types of eigenmodes of the unit cell, with different phase difference $\Delta\theta$ between cylinder A and cylinder B : one is in-phase $\Delta\theta = 0$ and the other one is anti-phase $\Delta\theta = \pi$. The in-phase

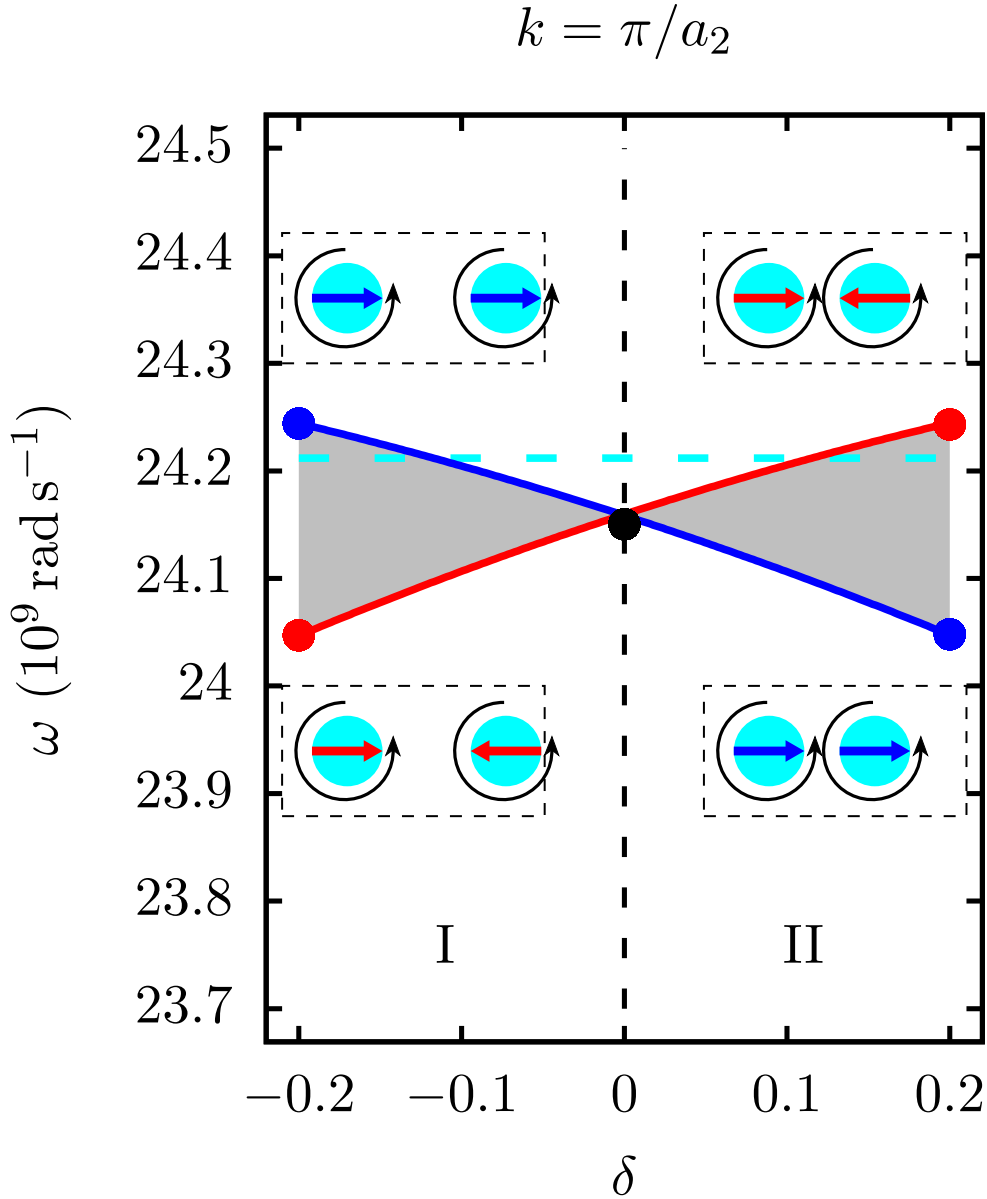


Figure 3.5: Band inversion and topological phase transition in dimer model of gyromagnetic cylinders on 1D infinite lattice. The curves are the upper and lower band edges at $k = \pi/a_2$ and the grey areas are the band gap. The eigenstate of the unit cell with $\delta = 0.2$ and $\delta = -0.2$ for both upper band and lower band are illustrated. The in-phase eigenmodes and the corresponding band are in blue, while the anti-phase eigenmodes and the corresponding band are in red. The cyan dashed line indicates the resonant frequency of a single gyromagnetic cylinder ω_0 . For $\delta < 0$, the system is in topological phase I, while for $\delta > 0$, it is in topological phase II. At $\delta = 0$, the system is gapless, which undergoes band inversion and topological phase transition.

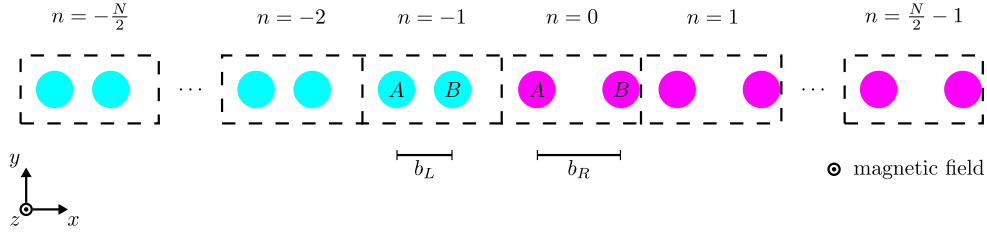


Figure 3.6: Illustration of 1D topological model of gyromagnetic lattices. The lattice constant is given by a_2 . The finite lattice composed of a left and a right part with different unit cells. The unit cells are indicated by the dashed boxes and indexed by the integer n . The distance between cylinder A and cylinder B , in the left and the right part of the lattice, is given by $b_L = (1 - \delta_L)a_2/2$ and $b_R = (1 - \delta_R)a_2/2$, respectively.

eigenmodes and the corresponding band are in blue, while the anti-phase eigenmodes and the corresponding band are in red. It is shown that, as δ varies and cross the point $\delta = 0$, the band with in-phase eigenmodes becomes anti-phase and vice versa. This observation illustrates band inversion and indicates topological phase transition in the dimer model. For $\delta < 0$, the system is in topological phase I, while for $\delta > 0$, it is in topological phase II. At $\delta = 0$, the system is gapless which undergoes band inversion and topological phase transition.

3.2.3 Finite lattice and topological edge modes

To demonstrate topological edge modes supporting in 1D gyromagnetic system, we consider a dimer model of gyromagnetic cylinders on 1D finite lattice in x -direction with lattice constant $a_2 = 18.75$ mm. The finite lattice composed of a left and a right part with different unit cells. For both the left and

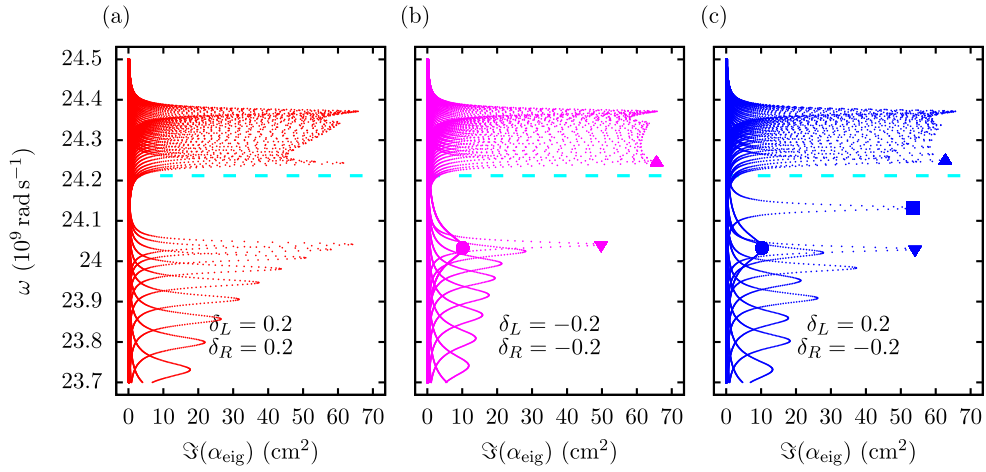


Figure 3.7: Band structures of dimer model of gyromagnetic cylinders on 1D finite lattice. (a) The topologically trivial system with both $\delta_L = 0.2$ and $\delta_R = 0.2$. (b) The topologically non-trivial system with both $\delta_L = -0.2$ and $\delta_R = -0.2$. (c) The system with $\delta_L = 0.2$ and $\delta_R = -0.2$, where the left and the right part of the lattice are topologically trivial and non-trivial, respectively. The upper and the lower triangle indicate the upper and the lower bands, respectively. The circle and the square are the topological edge modes. The cyan dashed line indicates the resonant frequency of a single gyromagnetic cylinder ω_0 .

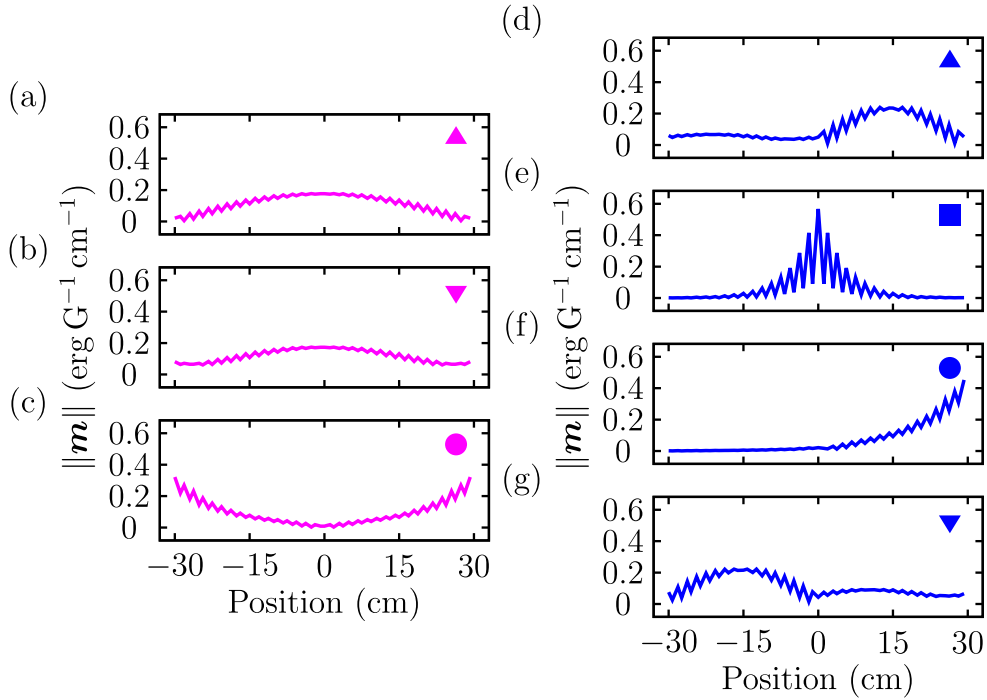


Figure 3.8: The norm of eigenmodes corresponding to the labeled modes in the band structures in Fig. 3.7. (a), (b), (c) The results for the system with $\delta_L = -0.2$ and $\delta_R = -0.2$. (d), (e), (f), (g) The results for the system with $\delta_L = 0.2$ and $\delta_R = -0.2$. In particular, (c), (e), and (f) are topological edge modes.

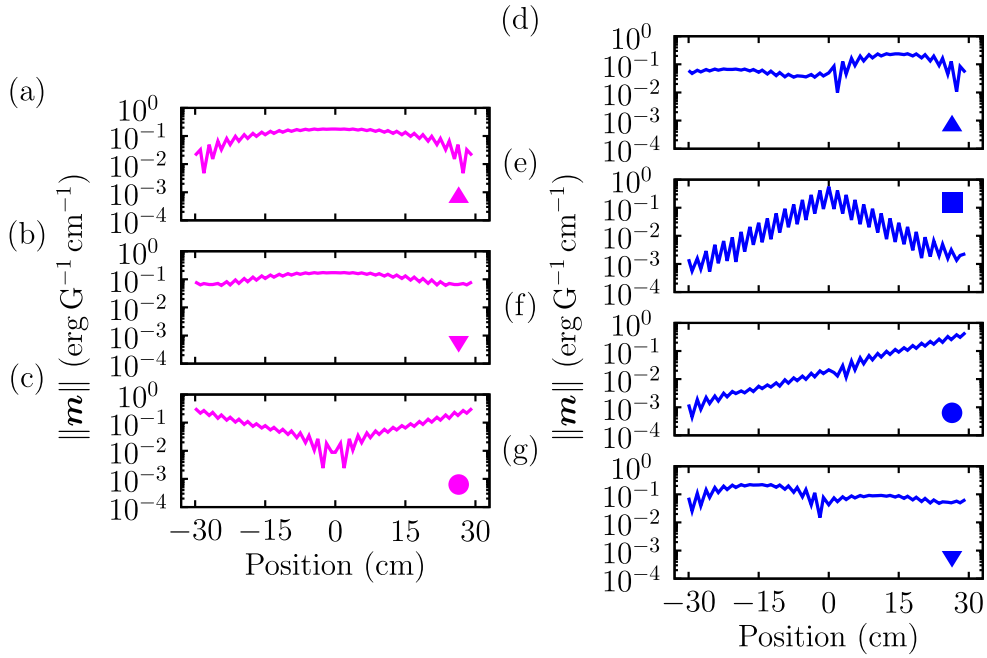


Figure 3.9: The norm of eigenmodes in semi-log plot corresponding to the labeled modes in the band structures in Fig. 3.7. (a), (b), (c) The results for the system with $\delta_L = -0.2$ and $\delta_R = -0.2$. (d), (e), (f), (g) The results for the system with $\delta_L = 0.2$ and $\delta_R = -0.2$. In particular, (c), (e), and (f) are topological edge modes.

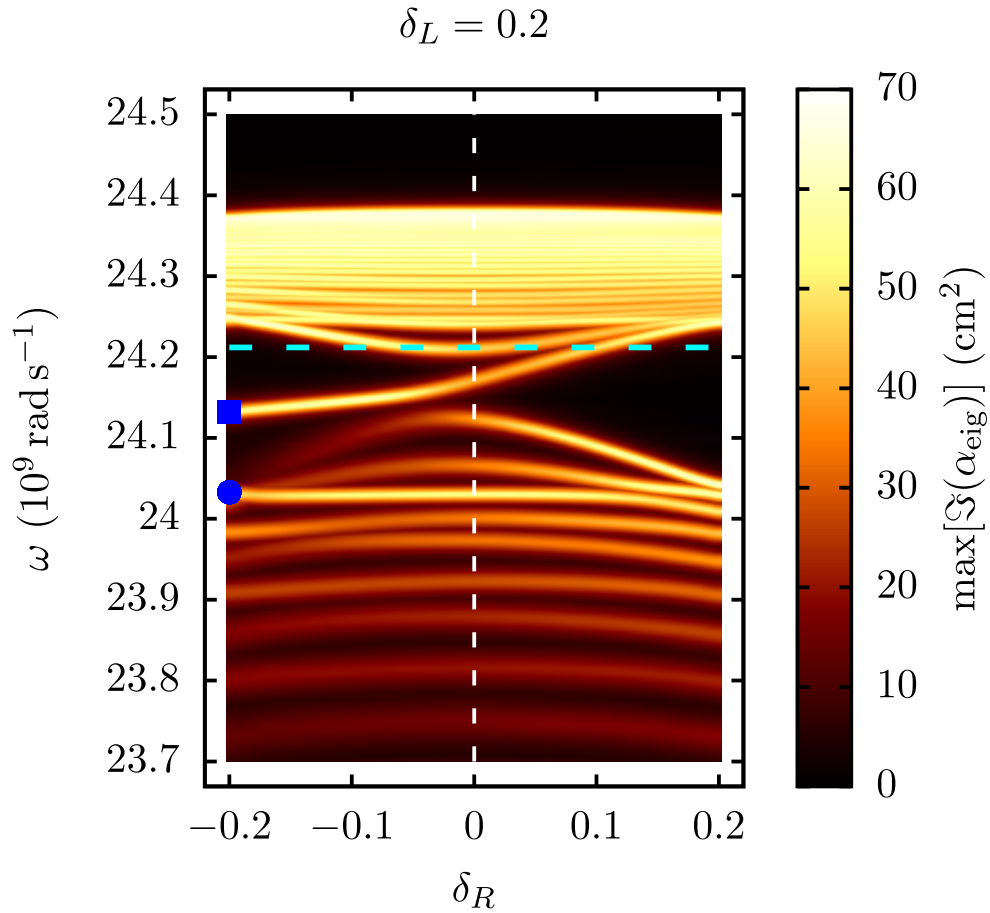


Figure 3.10: Topological phase transition of dimer model of gyromagnetic cylinders on 1D finite lattice with $\delta_L = 0.2$ and $\delta_R \in [-0.2, 0.2]$. The white dashed line at $\delta_R = 0$ indicates topological phase transition in the right part of the lattice and the cyan dashed line indicates the resonant frequency of a single gyromagnetic cylinder ω_0 . The blue square and the blue circle are the topological edge modes.

the right part of the lattice, the unit cell, indexed by the integer n , consists of two gyromagnetic cylinders labeled as A and B , with the same radius $r = 2.5$ mm as depicted in Fig. 3.6. We assume there are N unit cells with N being an even number, so $n = -N/2, \dots, 0, \dots, N/2 - 1$. Then $n < 0$ corresponds to the left part and $n \geq 0$ corresponds to the right part of the lattice. The displacement from cylinder A to B in unit cell n is given by $\mathbf{b}_n = b_n \hat{\mathbf{x}}$, where

$$b_n = \begin{cases} b_L & \text{if } n < 0, \\ b_R & \text{if } n \geq 0, \end{cases} \quad (3.25)$$

with

$$b_L = \frac{a_2}{2}(1 - \delta_L), \quad (3.26a)$$

$$b_R = \frac{a_2}{2}(1 - \delta_R). \quad (3.26b)$$

In the n th unit cell, the magnetic dipole moments is $\mathbf{m}_n = (\mathbf{m}_{n,A}, \mathbf{m}_{n,B})^T$ and the polarizability is $\boldsymbol{\alpha}_n(\omega) = \text{diag}(\boldsymbol{\alpha}_{n,A}, \boldsymbol{\alpha}_{n,B})$. Then we have $\tilde{\mathbf{m}} = (\mathbf{m}_{-N/2}, \dots, \mathbf{m}_0, \dots, \mathbf{m}_{N/2-1})^T$ and $\tilde{\boldsymbol{\alpha}}(\omega) = \text{diag}(\boldsymbol{\alpha}_{-N/2}, \dots, \boldsymbol{\alpha}_0, \dots, \boldsymbol{\alpha}_{N/2-1})$. We define $\tilde{\boldsymbol{\Gamma}}(\omega)$ as the interactions between the unit cells i and unit cell j , such that for $i = j$,

$$\tilde{\boldsymbol{\Gamma}}_{ij} = 4\pi k_0^2 \begin{pmatrix} \mathbf{0} & \mathbf{G}(0, \mathbf{b}_i) \\ \mathbf{G}(0, -\mathbf{b}_i) & \mathbf{0} \end{pmatrix}, \quad (3.27)$$

and for $i \neq j$

$$\tilde{\Gamma}_{ij} = 4\pi k_0^2 \begin{pmatrix} \mathbf{G}(0, \mathbf{R}_{ij}) & \mathbf{G}(0, \mathbf{R}_{ij} + \mathbf{b}_i) \\ \mathbf{G}(0, \mathbf{R}_{ij} - \mathbf{b}_i) & \mathbf{G}(0, \mathbf{R}_{ij}) \end{pmatrix}, \quad (3.28)$$

where $\mathbf{R}_{ij} := (j - i)a_2\hat{\mathbf{x}}$ is the displacement from unit cell i to unit cell j . Furthermore, we define

$$\tilde{\mathbf{M}}_{\text{dimer}}(\omega) := \tilde{\boldsymbol{\alpha}}^{-1}(\omega) - \tilde{\Gamma}(\omega). \quad (3.29)$$

The coupled-dipole equations for the dimer model of gyromagnetic cylinders on 1D finite lattice can be written as

$$\tilde{\mathbf{M}}_{\text{dimer}}(\omega)\tilde{\mathbf{m}} = 0, \quad (3.30)$$

where $\tilde{\mathbf{M}}_{\text{dimer}}(\omega)$ is a $4N \times 4N$ matrix. Finally, we have the eigenvalue problem

$$\tilde{\mathbf{M}}_{\text{dimer}}(\omega)\tilde{\mathbf{m}}_i = \lambda_i(\omega)\tilde{\mathbf{m}}_i, \quad (3.31)$$

with eigen-response theory described in Sec. 2.4.

We consider the finite lattice with $N = 32$. First, we study the topological trivial case with both $\delta_L = 0.2$ and $\delta_R = 0.2$. This is the finite case of the dimer model studied in Sec. 3.2.1 with $\delta = 0.2$. To clearly show the eigenmodes, we plot the quantity $\Im(\alpha_{\text{eig}})$. The result is shown in Fig. 3.7 (a). We found that there are two sets of modes correspond to the upper

and the lower band of the system. There is no state within the band gap, as expected. The results are in good agreement with the band structure obtained in Fig. 3.4 (d).

Next, we consider the topological non-trivial case with both $\delta_L = -0.2$ and $\delta_R = -0.2$. As is well known from the conventional SSH model, this system should present topological edge modes at the end of the chain by the bulk-boundary correspondence. The result is shown in Fig. 3.7 (b). Again, we observed that there are two sets of modes correspond to the upper and the lower band of the system. The bottom of the upper band is labeled by the magenta upper triangle and the top of the lower band is labeled by the magenta lower triangle. However, in contrast to the trivial case, there is a localized mode on the top of the lower band, which is labeled by the magenta circle. Then we calculated the corresponding norm of the eigenmodes $\|\mathbf{m}\| = \sqrt{\mathbf{m}^* \mathbf{m}}$ of the system. The results for the upper and lower band are shown in Fig. 3.9 (a) and (b), respectively. They are the usual normal modes of the system. For the localized mode on the top of the lower band, the norm of the eigenmodes is shown in Fig. 3.9 (c). We see that, this eigenmode localized at $\mathbf{m}_{-N/2,A}$ and $\mathbf{m}_{N/2-1,B}$, which is at the end of the chain. This is the topological edge modes supporting in the system. Since the full band gap in the dimer model only appears when dynamic long-range interactions are included and cannot be predicted by the tight-binding approach, it is very interesting to see that the dynamic long-range interactions lead to localized topological edge modes.

Furthermore, from the results in Fig. 3.5, we choose the two extreme cases with $\delta_L = 0.2$ and $\delta_R = -0.2$. Then the left part of the lattice is in topological phase II, while the right part of the lattice is in topological phase I. The result is shown in Fig. 3.7 (c). Again, we observed the upper and the lower band of the system, which are labeled by the upper blue triangle and the lower blue triangle, respectively. Besides the localized mode on the top of the lower band, which is labeled by the blue circle, there is also a localized mode at the center of the band gap, which is labeled by the blue square. There are two topological edge modes supporting in this system. The corresponding eigenmodes for the upper and the lower band are shown in Fig. 3.9 (d) and (g), respectively. The eigenmodes are neither symmetric nor anti-symmetric about the center of the chain because the system has a broken inversion and reflection symmetry. For the localized mode on the top of the lower band, the norm of the eigenmode is shown in Fig. 3.9 (f). Now, this eigenmodes only localized at $\mathbf{m}_{N/2-1,B}$, which is the right end of the chain. For the localized mode at the center of the band gap, the norm of the eigenmode is shown in Fig. 3.9 (e). It is shown that, this eigenmode localized at $\mathbf{m}_{0,A}$, which is the boundary between the left and the right part of the lattice. As long as the left part and the right part of the lattice are in two distinct topological phases, protected modes exist at the boundary where there is topological phase transition.

To study the effects of dynamic long-range interactions on the topological edge modes, we consider the system with fixed $\delta_L = 0.2$, and $\delta_R \in [-0.2, 0.2]$.

The band structures are shown in Fig. 3.10. For $\delta_R > 0$, both the left and the right part of the lattice are in the same topological phase II. As a result, there is no mode within the band gap in the system. We observed that, as δ_R decrease from $\delta_R = 0.2$, the band gap becomes smaller. When the system crossing $\delta_R = 0$, which is indicated by the white dashed line, the right part of the lattice undergoes topological phase transition, as discussed in Sec. 3.2.2. Hence, for $\delta_R < 0$, the right part of the lattice is in topological phase I. Now, the left and the right part of the lattice are in two distinct topological phases. By the prediction of the bulk-boundary correspondence, topological edge modes will exist. We observed that, after the system crossing $\delta_R = 0$, the topological edge mode emerges from the bottom of the upper band and it is redshifted from the resonant frequency of a single gyromagnetic cylinder ω_0 .

In the conventional SSH model and its analogous systems, the topological edge modes can be predicted by the bulk-boundary correspondence with a tight-binding approach in quasi-static limit, where only nearest-neighbor interactions are being considered. However, this is not possible with our 1D topological model for gyromagnetic system. As seen in Fig. 3.4 (c), in quasi-static limit, apart from not having a full band gap, the resonant frequency of a single gyromagnetic cylinder ω_0 , which corresponds to the zero-energy state in the SSH model, is on top of the bands. Since the chiral symmetry ensures the spectral position of any edge mode lies at ω_0 , the topological nature of edge mode is not well defined. As discussed in Sec. 3.2.1, in order to obtain

a full band gap, the dynamic long-range interactions have to be taken into account. Furthermore, chiral symmetry of the system is broken due to the dynamic long-range interactions[44, 45], the topological edge modes are red-shifted from ω_0 , such that they are within two topological bands and can be understood by the bulk-boundary correspondence. Therefore, the dynamic long-range interaction plays a crucial role in opening a band gap and supporting the topological edge modes in our system. The details of finite lattice in quasi-static limit is presented in Appendix C. Part of the band structures and edge modes (or density of states) of this topological 1D array of gyromagnetic cylinders could be verified experimentally through measurement of the transmission along the chain using near-field techniques[72, 73, 74, 7].

Chapter 4

One-dimensional (1D) gyroelectric lattices

In this chapter, the results for 1D array of strongly dispersive gyroelectric resonant cylinders are presented. The structure of the chapter is analogous to Chapter 3. The objective is to show the differences between gyromagnetic and gyroelectric systems. It should be noted that, SI unit is used in this chapter.

4.1 Regular chain

4.1.1 Infinite lattice

We begin by considering a 1D infinite lattice with lattice constant $a_1 = 0.9375 \mu\text{m}$ in x -direction as depicted in Fig. 4.1. The unit cell consists of

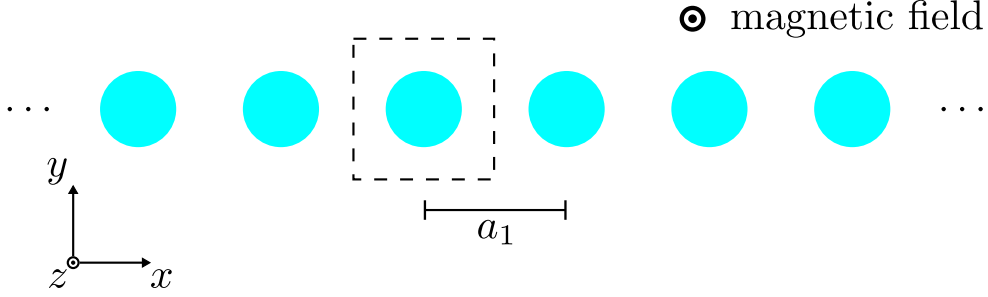


Figure 4.1: Illustration of gyroelectric cylinders on 1D infinite lattice. The lattice constant is given by a_1 . The unit cell is indicated by the dashed box. The size of the gyroelectric system is 10^4 times smaller than the gyromagnetic one considered in Chapter 3.

one gyroelectric cylinder with radius $r = 0.25 \mu\text{m}$ and axis of the cylinder in z -direction. The size of the gyroelectric system is 10^4 times smaller than the gyromagnetic one considered in Chapter 3. The parameters are chosen with $a_1 \geq 3r$, such that the cylinders are not too close to each other. For frequencies near the dipole resonance, we take the dipole approximation, in which each cylinder is treated as a point dipole[5]. We are interested in the fields of the dipole moments in the xy -plane, which are perpendicular to the axis of the cylinder. The polarizability of a cylinder is given by[66]

$$\boldsymbol{\alpha}^{-1}(\omega) = \frac{1}{\epsilon_0 A} \left(\left[\frac{\boldsymbol{\epsilon}(\omega)}{\epsilon_0} - \mathbf{I} \right]^{-1} + \mathbf{L} \right) - i \frac{k_0^2}{8\epsilon_0} \mathbf{I}, \quad (4.1)$$

where $A = \pi r^2$, \mathbf{I} is the 2×2 identity matrix, and $\mathbf{L} = (1/2)\mathbf{I}$ is the depolarization factors for cylinder, $k_0 = \omega/c$ is the wavenumber in the background medium and $\boldsymbol{\epsilon}(\omega)$ is the permittivity tensor of the gyroelectric medium. The radiative correction term $-i(k_0^2/8\epsilon_0)\mathbf{I}$ is included to satisfy the optical theo-

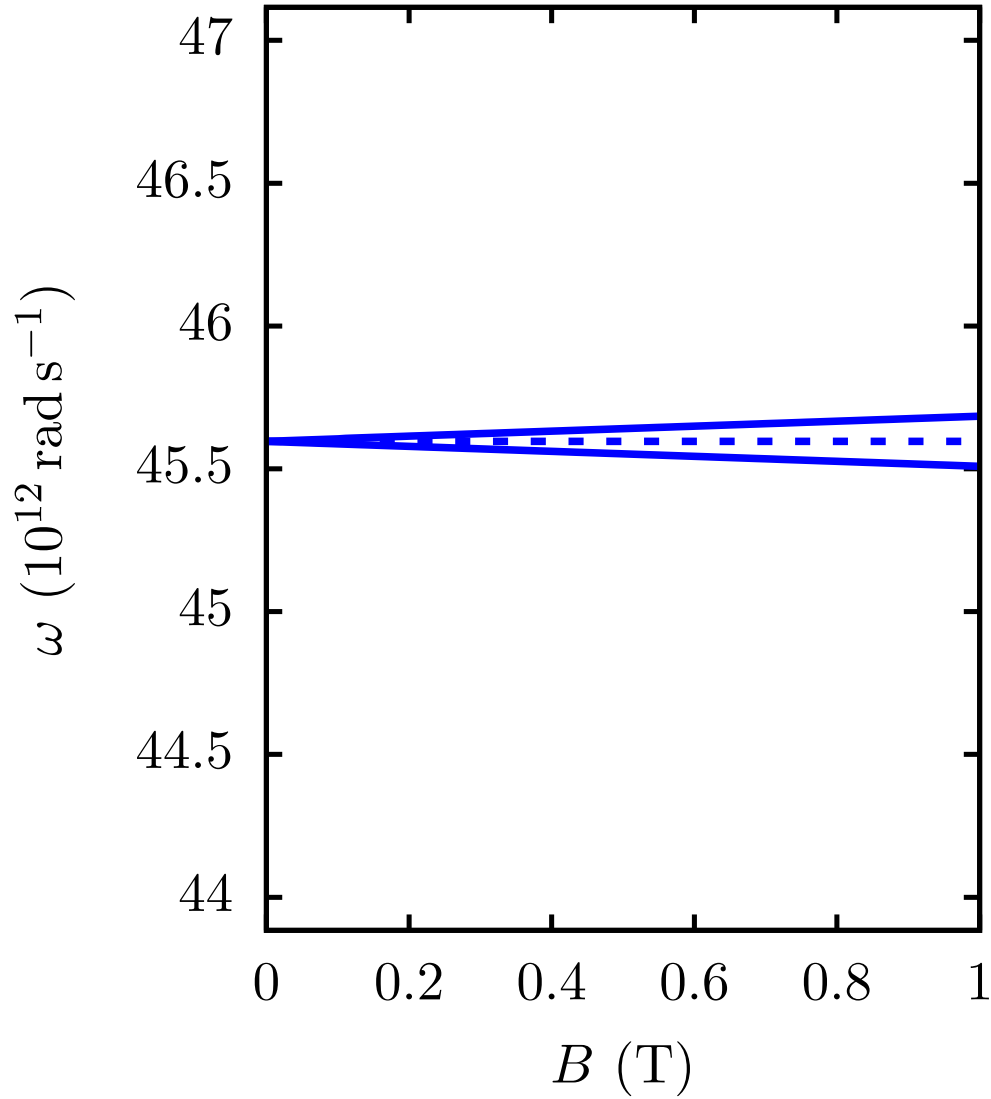


Figure 4.2: The splitting of resonant frequency of a single gyroelectric cylinder ω_0 in the presence of applied static magnetic field B . The blue dotted line indicated the resonant frequency $\omega_0 = \omega_p/\sqrt{2}$ for $B = 0$. Two two blue lines correspond to the splitted resonant frequency $\omega_{0,+}$ and $\omega_{0,-}$.

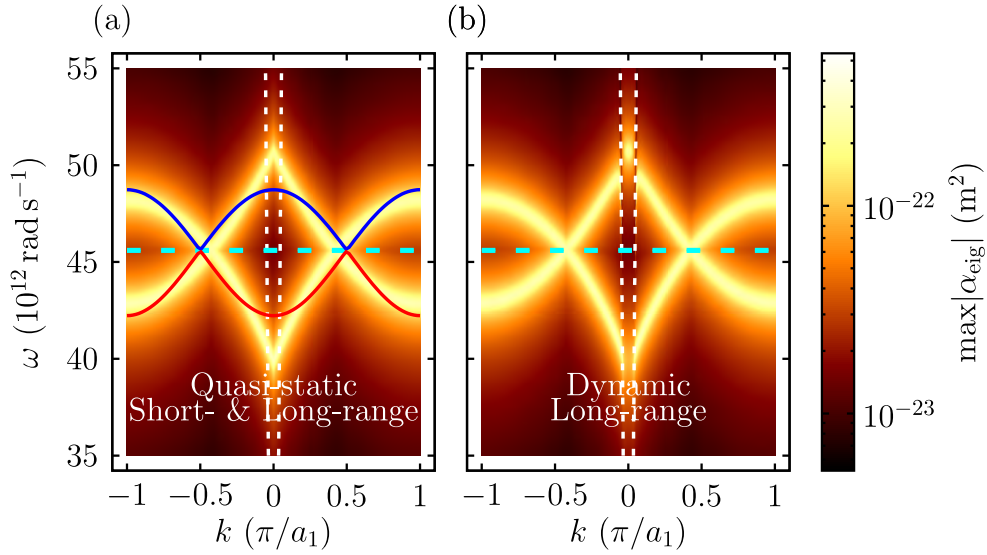


Figure 4.3: (a) The photonic band structure with short- and long-range interactions in quasi-static limit. The blue and red lines are the dispersion relation with nearest-neighbor interactions only. (b) The photonic band structure with dynamic long-range interactions. The white dotted lines are the light lines and the region within the light lines is the light cone. The cyan dashed line indicates the resonant frequency of a single gyroelectric cylinder $\omega_{0,\pm}$. All results are calculated with $B = 0.5 \text{ T}$.

rem. For the case that the applied static magnetic field \mathbf{B} are parallel to the axis of the cylinder in $+z$ -direction, the permittivity tensor is given by[12]

$$\frac{\boldsymbol{\epsilon}(\omega)}{\epsilon_0} = \begin{pmatrix} \epsilon_1 & -i\epsilon_2 \\ i\epsilon_2 & \epsilon_1 \end{pmatrix}, \quad (4.2)$$

with

$$\epsilon_1 = 1 - \frac{\omega_p^2(\omega + i\beta)}{\omega(\omega + i\beta)^2 - \omega\omega_c^2}, \quad (4.3a)$$

$$\epsilon_2 = \frac{\omega_p^2\omega_c}{\omega(\omega + i\beta)^2 - \omega\omega_c^2}, \quad (4.3b)$$

where ω_p is the plasma frequency, β is the electron collision frequency, and $\omega_c = eB/m_e$ is the cyclotron frequency, in which e is the elementary charge, and m_e is the electron rest mass. We consider the cylinders are made of intrinsic indium antimonide (InSb), which is a semiconductor with properties depending on temperature T . The plasma frequency of intrinsic InSb is given by[75]

$$\omega_p^2 = \sum_i \frac{n_i e^2}{m_i \epsilon_0} \quad (4.4)$$

where n_i is the densities and m_i is the effective masses of the free electrons and holes in the relevant conduction and valence bands i . The density of free electron of intrinsic Insb is given by

$$n_e = 5.76 \times 10^{20} T^{3/2} e^{\frac{-0.13}{k_B T}} \quad (4.5)$$

where T in K, $k_B T$ in eV, and n_e in m^{-3} . The parameters we used are $T = 300$ K and $\beta = 0.01\omega_p$. From these expressions, we have

$$\boldsymbol{\alpha}^{-1}(\omega) = \begin{pmatrix} \frac{1}{\pi\epsilon_0 r^2} \left(\frac{1}{2} - \frac{\omega^2}{\omega_p^2} - i \frac{\beta\omega}{\omega_p^2} \right) - i \frac{k_0^2}{8\epsilon_0} & i \frac{1}{\pi\epsilon_0 r^2} \left(\frac{\omega\omega_c}{\omega_p^2} \right) \\ -i \frac{1}{\pi\epsilon_0 r^2} \left(\frac{\omega\omega_c}{\omega_p^2} \right) & \frac{1}{\pi\epsilon_0 r^2} \left(\frac{1}{2} - \frac{\omega^2}{\omega_p^2} - i \frac{\beta\omega}{\omega_p^2} \right) - i \frac{k_0^2}{8\epsilon_0} \end{pmatrix}. \quad (4.6)$$

The resonant frequency of a single gyroelectric cylinder $\omega_{0,\pm}$ is found by solving $\Re[\det \boldsymbol{\alpha}^{-1}(\omega_{0,\pm})] = 0$, which gives

$$\omega_{0,\pm} = \frac{1}{2} \left(\sqrt{\omega_c^2 + 2\omega_p^2} \pm \omega_c \right). \quad (4.7)$$

For $B = 0.5$ T, it is equal to $f_{0,+} = \omega_{0,+}/(2\pi) = 7.264$ THz, and $f_{0,-} = \omega_{0,-}/(2\pi) = 7.245$ THz which is in the terahertz regime. For $\mathbf{B} = 0$, we have

$$\omega_0 = \frac{\omega_p}{\sqrt{2}}, \quad (4.8)$$

which is equal to $f_0 = \omega_0/(2\pi) = 7.257$ THz. As discussed in Chapter 3, ω_0 can be interpreted as the spectral position of the zero-energy state in the SSH model in gyromagnetic systems. However, in gyroelectric systems, it is splitted into two resonant frequencies $\omega_{0,+}$ and $\omega_{0,-}$. The splitting of ω_0 with magnetic field B is shown in Fig. 4.2.

For our system, we have the 2D Green's tensor[61]

$$\mathbf{G}(\boldsymbol{\rho}, \boldsymbol{\rho}') = \begin{pmatrix} G_{xx} & 0 \\ 0 & G_{yy} \end{pmatrix}, \quad (4.9)$$

with

$$G_{xx} = \frac{i}{4} \left(\frac{1}{k_0 R} \right) H_1^{(1)}(k_0 R), \quad (4.10a)$$

$$G_{yy} = \frac{i}{4} \left(H_0^{(1)}(k_0 R) - \frac{1}{k_0 R} H_1^{(1)}(k_0 R) \right), \quad (4.10b)$$

where $\mathbf{R} := \boldsymbol{\rho}' - \boldsymbol{\rho}$ is the relative displacement between the source and the observation points, and $H_i^{(1)}$ is the Hankel function of the first kind.

We have the following coupled-dipole equations, which is analog to that describing gyromagnetic system, given by

$$\mathbf{p}(\boldsymbol{\rho}) = \boldsymbol{\alpha}(\omega) \left(\frac{k_0^2}{\epsilon_0} \sum_{\boldsymbol{\rho}' \neq \boldsymbol{\rho}} \mathbf{G}(\boldsymbol{\rho}, \boldsymbol{\rho}') \mathbf{p}(\boldsymbol{\rho}') + \mathbf{E}_0(\boldsymbol{\rho}) \right), \quad (4.11)$$

where the sum includes all the dipole moments except the self-interaction term and $\mathbf{E}_0(\boldsymbol{\rho})$ is the external excitation electric field. For example, \mathbf{E}_0 can be the field of a plane wave.

For 1D infinite lattice, the translational symmetry leads to Bloch's theorem

$$\mathbf{p}(\boldsymbol{\rho} + \mathbf{R}) = e^{i\mathbf{k} \cdot \mathbf{R}} \mathbf{p}(\boldsymbol{\rho}), \quad (4.12)$$

where the displacement $\mathbf{R} = na_1\hat{\mathbf{x}}$, with integer n and lattice constant a_1 , and the wave vector $\mathbf{k} = k\hat{\mathbf{x}}$, with the first Brillouin zone $k \in [-\pi/a_1, \pi/a_1]$. Also, we have $\mathbf{G}(\boldsymbol{\rho}, \boldsymbol{\rho}') = \mathbf{G}(0, \mathbf{R})$. The coupled-dipole equation for infinite lattice is given by

$$\mathbf{p}(\boldsymbol{\rho}) = \boldsymbol{\alpha}(\omega) \left(\frac{k_0^2}{\epsilon_0} \sum_{\mathbf{R} \neq 0} \mathbf{G}(0, \mathbf{R}) e^{i\mathbf{k} \cdot \mathbf{R}} \mathbf{p}(\boldsymbol{\rho}) + \mathbf{E}_0(\boldsymbol{\rho}) \right), \quad (4.13)$$

and we define

$$\mathbf{M}(\mathbf{k}, \omega) := \boldsymbol{\alpha}^{-1}(\omega) - \frac{k_0^2}{\epsilon_0} \sum_{\mathbf{R} \neq 0} \mathbf{G}(0, \mathbf{R}) e^{i\mathbf{k} \cdot \mathbf{R}}. \quad (4.14)$$

The translational symmetry reduces \mathbf{M} to a 2×2 matrix. Then Eq. (4.13) can be rewritten as

$$\mathbf{M}(\mathbf{k}, \omega) \mathbf{p} = \mathbf{E}_0. \quad (4.15)$$

Then the eigenvalue problem for infinite lattice is

$$\mathbf{M}(\mathbf{k}, \omega) \mathbf{p}_i = \lambda_i(\mathbf{k}, \omega) \mathbf{p}_i. \quad (4.16)$$

It should be noted that, \mathbf{M} is non-Hermitian due to the loss and dynamic effects. From now on, we set $\mathbf{E}_0 = 0$, so as to study the normal modes of the system.

Quasi-static limit

We calculate the band structure of the gyroelectric system described in Sec. 4.1.1 in an infinite lattice. Before studying the more general case, we consider the system in quasi-static limit $k_0 \rightarrow 0$. The coupled-dipole equations in quasi-static limit is analog to those described in Appendix A. From Eq. (A.10), we have

$$\mathbf{M}'(\mathbf{k}, \omega) = \frac{1}{4\pi\epsilon_0} \begin{pmatrix} \frac{4}{r^2} \left(\frac{1}{2} - \frac{\omega^2}{\omega_p^2} - i \frac{\beta\omega}{\omega_p^2} \right) - \sum_{\mathbf{R} \neq 0} \frac{2}{R^2} e^{i\mathbf{k} \cdot \mathbf{R}} & i \frac{4}{r^2} \left(\frac{\omega\omega_c}{\omega_p^2} \right) \\ -i \frac{4}{r^2} \left(\frac{\omega\omega_c}{\omega_p^2} \right) & \frac{4}{r^2} \left(\frac{1}{2} - \frac{\omega^2}{\omega_p^2} - i \frac{\beta\omega}{\omega_p^2} \right) + \sum_{\mathbf{R} \neq 0} \frac{2}{R^2} e^{i\mathbf{k} \cdot \mathbf{R}} \end{pmatrix}. \quad (4.17)$$

Then, the system is described by

$$\mathbf{M}'(\mathbf{k}, \omega) \mathbf{p} = 0. \quad (4.18)$$

Now, we take the tight-binding approach, in which only short-range interactions are being considered. By including only the nearest-neighbor interactions, the dispersion relation and the normal mode can be obtained analytically by solving the non-trivial solution of Eq. (3.15). From $\Re[\det \mathbf{M}'(\mathbf{k}, \omega)] = 0$, we obtain the dispersion relations, we have

$$\omega(k) = \sqrt{\frac{\omega_p^2 + \omega_c^2}{2}} \pm \sqrt{\omega_c^2(2\omega_p^2 + \omega_c^2) + 4\omega_p^4 f(k)^2}, \quad (4.19)$$

with

$$f(k) := \left(\frac{r}{a_1}\right)^2 \cos(ka_1), \quad (4.20)$$

For $\mathbf{B} = 0$, it becomes

$$\omega(k) = \frac{\omega_p}{\sqrt{2}} (1 \pm f(k)), \quad (4.21)$$

where at $k = \pm\pi/(2a_1)$, the two bands are degenerate. For $B = 0.5 \text{ T}$, they are plotted with blue and red lines in Fig. 4.3 (a). We observe two bands, instead of one in gyromagnetic system. The presence of magnetic field breaks the time-reversal symmetry and the degeneracies are splitted. We see that two non-trivial solution is obtained from the 2×2 matrix problem of Eq. (4.18). At $k = \pm\pi/a_1$, the upper band is the longitudinal mode and the lower band is the transverse mode. Different from the gyromagnetic systems, the longitudinal mode and the transverse mode are not coupled. Both the longitudinal mode and the transverse mode of the system do not couple to the photon mode of the background medium. Although the resonant frequency of a single gyroelectric cylinder ω_0 splits into $\omega_{0,\pm}$, there spectral positions are very close. The band structure is symmetric about the resonant frequency of a single gyroelectric cylinder $\omega_{0,\pm}$. The group velocity $v_g = d\omega/dk$ of both the transverse mode and the longitudinal mode is zero, $v_g = 0$, at $k = 0, \pm\pi/a_1$.

We consider the system in quasi-static limit including long-range interac-

tions. Now, we have the eigenvalue problem

$$\mathbf{M}'(\mathbf{k}, \omega) \mathbf{m}_i = \lambda_i(\mathbf{k}, \omega) \mathbf{m}_i, \quad (4.22)$$

where $\mathbf{M}'(\mathbf{k}, \omega)$ is given by Eq. (4.17). The band structure is shown in Fig. 4.3. We see that, the general features of the bands are similar to the results obtained with short-range interaction, except at the Brillouin zone center $k = 0$, where the group velocity v_g becomes discontinuous. We will soon show that the results obtained in quasi-static limit already give good description to the qualitative features of the system.

Dynamic long-range interaction

Now, we extend our calculation to include the dynamic long-range interactions. We consider the non-Hermitian eigenvalue problem of Eq. (4.16) with eigen-response theory. The band structure can be obtained from the peaks of $\max|\alpha_{\text{eig}}|$ and it is shown in Fig. 4.3 (b).

The result is very similar to the results calculated with either short-range interactions, or long-range interactions, in quasi-static limit. The only difference is that, both the longitudinal mode and the transverse mode of the system coupled strongly to the photon mode of the background medium. The band forms outside the light cone with $|k| > \omega/c$, which represent guided modes and any mode in the light cone with $|k| < \omega/c$ is radiation mode[69].

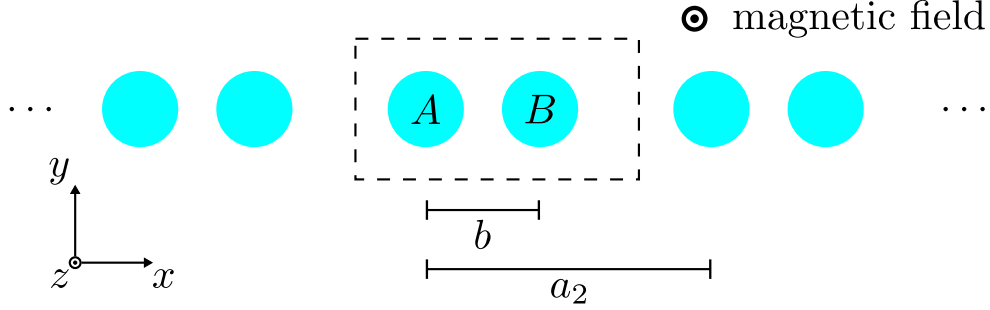


Figure 4.4: Illustration of dimer model of gyroelectric cylinders on 1D infinite lattice. The lattice constant is given by a_2 . The unit cell is indicated by the dashed box. The distance between cylinder A and cylinder B is given by $b = (1 - \delta)a_2/2$. The size of the gyroelectric system is 10^4 times smaller than the gyromagnetic one considered in Chapter 3.

4.2 Dimerized chain

4.2.1 Model

To further compare the difference between gyroelectric systems and gyromagnetic systems, we consider a dimer model of gyroelectric cylinders on 1D infinite lattices. In this dimer model, the lattice constant is given by $a_2 = 2a_1 = 1.875 \mu\text{m}$. The unit cell consists of two gyroelectric cylinders, labeled as A and B , with the same radius $r = 0.25 \mu\text{m}$. The displacement from cylinder A to cylinder B is given by $\mathbf{b} = b\hat{\mathbf{x}}$, with

$$b = \frac{a_2}{2}(1 - \delta), \quad (4.23)$$

where δ is a dimensionless parameter with $|\delta| \leq 0.2$ and hence $b \geq 3r$. The system is depicted in Fig. 4.4. The polarizability for cylinder A and cylinder

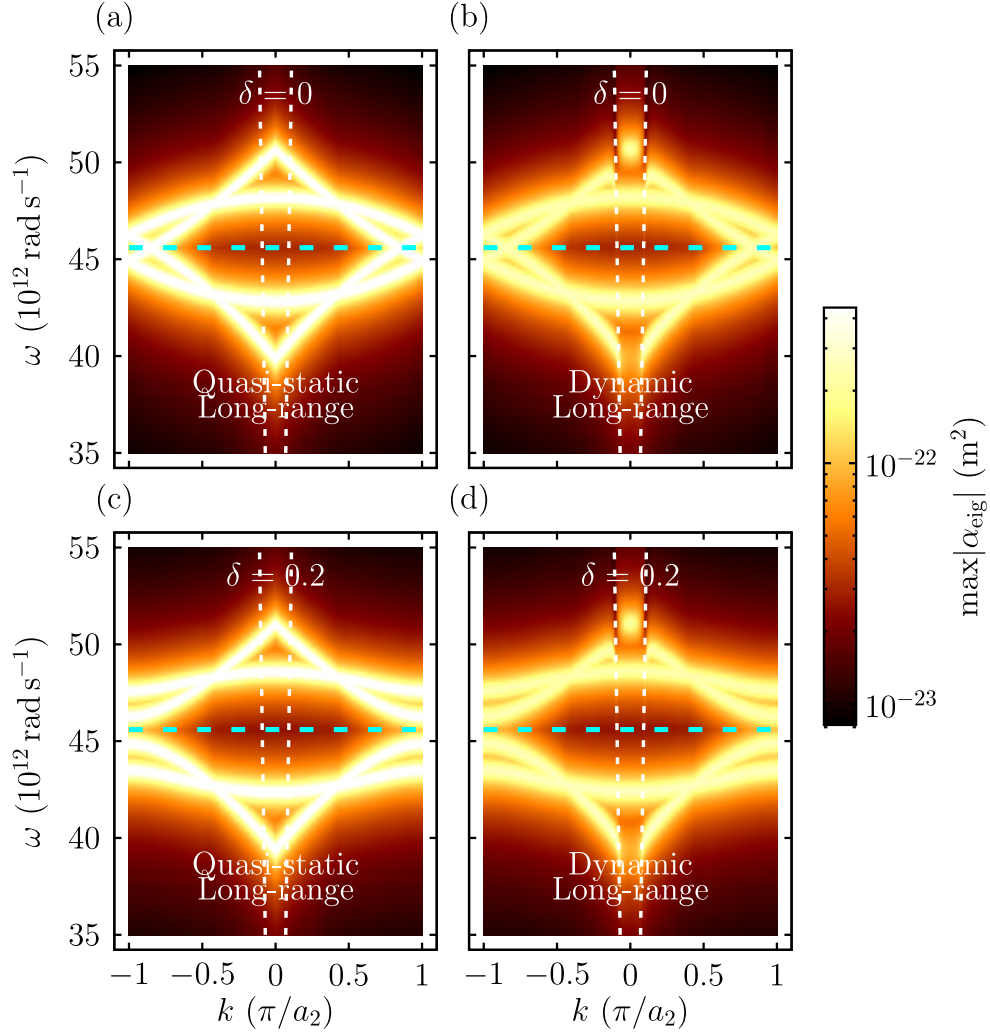


Figure 4.5: (a), (b), (c), (d) The photonic band structure for dimer model with $B = 0.5$ T in quasi-static limit and in general, with dynamic effects. All results include the long-range interactions. The white dotted lines are the light lines and the region within the light lines is the light cone. The cyan dashed line indicates the resonant frequency of a single gyroelectric cylinder $\omega_{0,\pm}$.

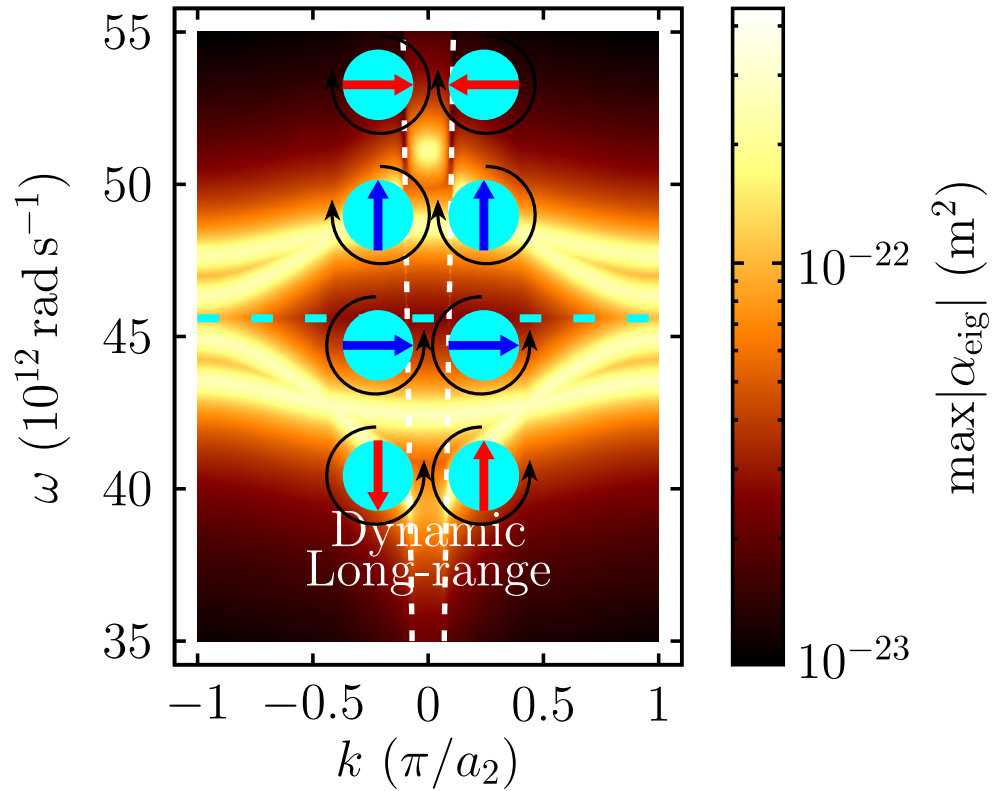


Figure 4.6: The normal modes in the dimerized chain. The photonic band structure for dimer model with dynamic long-range interactions. The eigenstate of the unit cell for each band is illustrated. The in-phase eigenmodes are in blue, while the anti-phase eigenmodes are in red. The white dotted lines are the light lines and the region within the light lines is the light cone. The cyan dashed line indicates the resonant frequency of a single gyroelectric cylinder $\omega_{0,\pm}$.

B are given by $\boldsymbol{\alpha}_A$ and $\boldsymbol{\alpha}_B$, and their corresponding electric dipole moments are given by \mathbf{p}_A and \mathbf{p}_B , respectively. With Bloch's theorem in Eq. (4.12), the coupled-dipole equations for the dimer model can be written as

$$\begin{pmatrix} \boldsymbol{\alpha}_A^{-1} & 0 \\ 0 & \boldsymbol{\alpha}_B^{-1} \end{pmatrix} \begin{pmatrix} \mathbf{p}_A \\ \mathbf{p}_B \end{pmatrix} = \boldsymbol{\Gamma} \begin{pmatrix} \mathbf{p}_A \\ \mathbf{p}_B \end{pmatrix}, \quad (4.24)$$

with

$$\boldsymbol{\Gamma} := \frac{k_0^2}{\epsilon_0} \begin{pmatrix} \sum_{\mathbf{R} \neq 0} \mathbf{G}(0, \mathbf{R}) e^{i\mathbf{k} \cdot \mathbf{R}} & \sum_{\mathbf{R}} \mathbf{G}(0, \mathbf{R} + \mathbf{b}) e^{i\mathbf{k} \cdot \mathbf{R}} \\ \sum_{\mathbf{R}} \mathbf{G}(0, \mathbf{R} - \mathbf{b}) e^{i\mathbf{k} \cdot \mathbf{R}} & \sum_{\mathbf{R} \neq 0} \mathbf{G}(0, \mathbf{R}) e^{i\mathbf{k} \cdot \mathbf{R}} \end{pmatrix}, \quad (4.25)$$

and the associated eigenvalue problem with eigen-response theory is given by

$$\mathbf{M}_{\text{dimer}}(\mathbf{k}, \omega) \mathbf{p}_i = \lambda_i(\mathbf{k}, \omega) \mathbf{p}_i, \quad (4.26)$$

where

$$\mathbf{M}_{\text{dimer}}(\mathbf{k}, \omega) := \begin{pmatrix} \boldsymbol{\alpha}_A^{-1} & 0 \\ 0 & \boldsymbol{\alpha}_B^{-1} \end{pmatrix} - \boldsymbol{\Gamma}, \quad (4.27)$$

is a non-Hermitian 4×4 matrix.

We consider the system with $\delta = 0$ and $\delta = 0.2$, in quasi-static limit (see Appendix B) and in general, with dynamic effects, all with long-range interactions. Again, the band structure can be obtained from the peaks of $\max|\alpha_{\text{eig}}|$. For $\delta = 0$, the system is the same as that discussed in Sec. 4.1.1

as depicted in Fig. 4.1. The band structures for this system are shown in Fig. 4.5 (a) and (b). Four bands are obtained due to the band folding and they are physically the same with those in Fig. 4.3 (a) and (b). In both cases, the results are gapless and there are two degeneracies at the Brillouin zone boundary $k = \pm\pi/a_2$ protected by the inversion symmetry of the system. For the case in quasi-static limit, the band structure is symmetric about the resonant frequency of a single gyroelectric cylinder $\omega_{0,\pm}$.

For $\delta = 0.2$, the band structures are shown in Fig. 4.5 (c) and (d). Again, four bands are obtained. For any $\delta \neq 0$, the inversion symmetry of the system is broken, hence the degeneracy split. For both the cases in quasi-static limit and with dynamic effects, the systems open a full band gap. Moreover, the band gap is approximately the same in both cases and the resonant frequency of a single gyroelectric cylinder $\omega_{0,\pm}$ is at the center of the band gap.

There are four normal modes in the dimer model, two transverse modes and two longitudinal modes, each with in-phase modes and anti-phase modes. The eigenmodes of each band are shown in Fig 4.6.

We showed that, for dimer model of gyroelectric cylinders on 1D infinite lattice, studying the system in quasi-static limit is suffice to obtained a full band gap, as long as inversion symmetry is broken in the system. Furthermore, for both results in quasi-static limit and with dynamic long-range interactions, the resonant frequency of a single gyroelectric cylinder $\omega_{0,\pm}$ is at the center of the band gap. This is a major difference with the gyromagnetic systems discussed in Chapter 3.

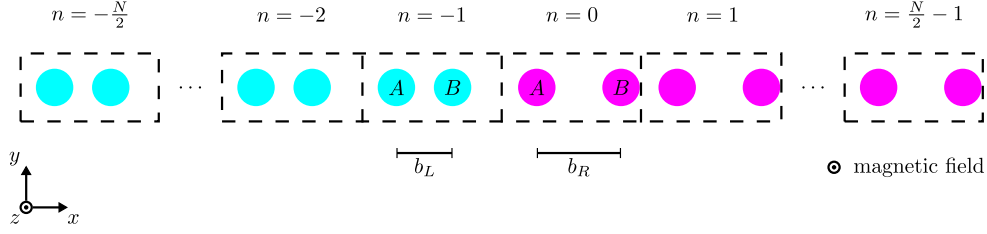


Figure 4.7: Illustration of 1D topological model of gyroelectric lattices. The lattice constant is given by a_2 . The finite lattice composed of a left and a right part with different unit cells. The unit cells are indicated by the dashed boxes and indexed by the integer n . The distance between cylinder A and cylinder B , in the left and the right part of the lattice, is given by $b_L = (1 - \delta_L)a_2/2$ and $b_R = (1 - \delta_R)a_2/2$, respectively. The size of the gyroelectric system is 10^4 times smaller than the gyromagnetic one considered in Chapter 3.

4.2.2 Finite lattice and topological edge modes

Following the discussion of the topological phase transition in the dimer model of gyromagnetic cylinders on 1D infinite lattices by the associated band inversion[71] in Chapter 3, we introduce the same concept into gyroelectric systems. Then, for $\delta < 0$, the system is in topological phase I, while for $\delta > 0$, it is in topological phase II. At $\delta = 0$, the system is gapless which undergoes band inversion and topological phase transition.

To demonstrate topological edge modes supporting in 1D gyroelectric system, we consider a dimer model of gyroelectric cylinders on 1D finite lattice in x -direction with lattice constant $a_2 = 1.875 \mu\text{m}$. The finite lattice composed of a left and a right part with different unit cells. For both the left and the right part of the lattice, the unit cell, indexed by the integer n , consists of two gyroelectric cylinders labeled as A and B , with the same

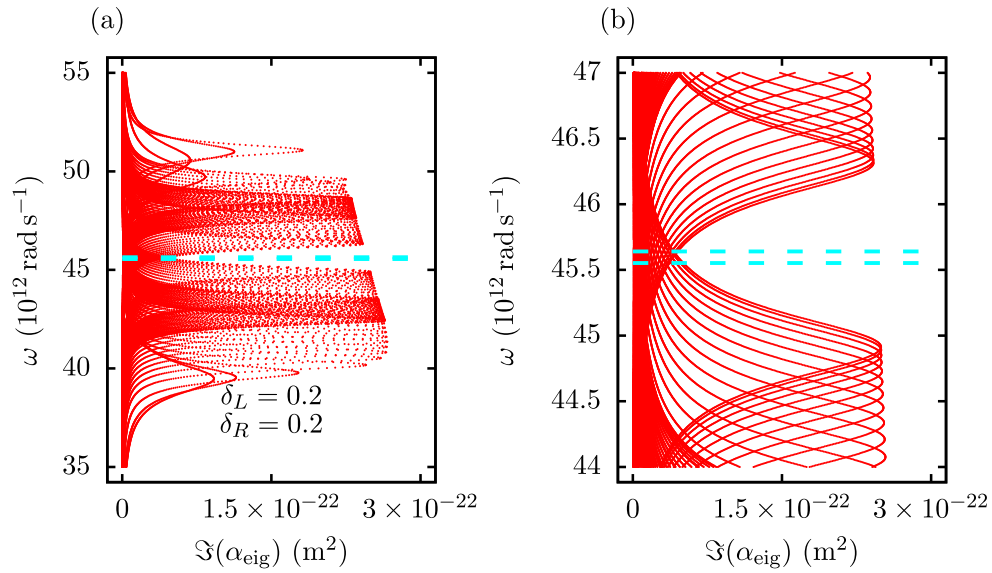


Figure 4.8: Band structures of dimer model of gyroelectric cylinders on 1D finite lattice with $B = 0.5 \text{ T}$. (a) The topologically trivial system with both $\delta_L = 0.2$ and $\delta_R = 0.2$. (b) The same band structure in high resolution. The cyan dashed line indicates the resonant frequency of a single gyroelectric cylinder $\omega_{0,\pm}$.

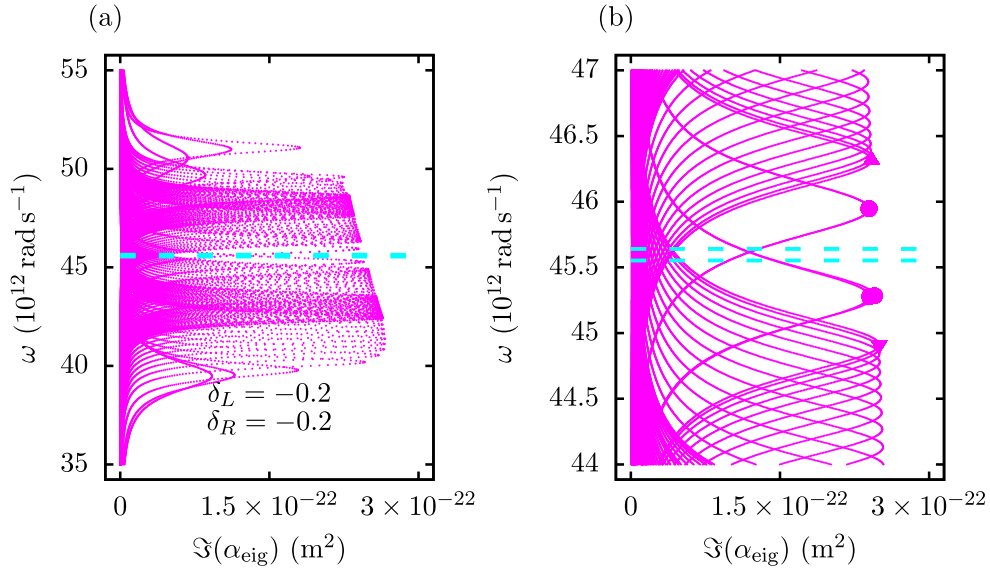


Figure 4.9: Band structures of dimer model of gyroelectric cylinders on 1D finite lattice with $B = 0.5$ T. (a) The topologically non-trivial system with both $\delta_L = -0.2$ and $\delta_R = -0.2$. (b) The same band structure in high resolution. The upper and the lower triangle indicate the upper and the lower bands, respectively. The circles are the topological edge modes each with two-fold degeneracy. The cyan dashed line indicates the resonant frequency of a single gyroelectric cylinder $\omega_{0,\pm}$.

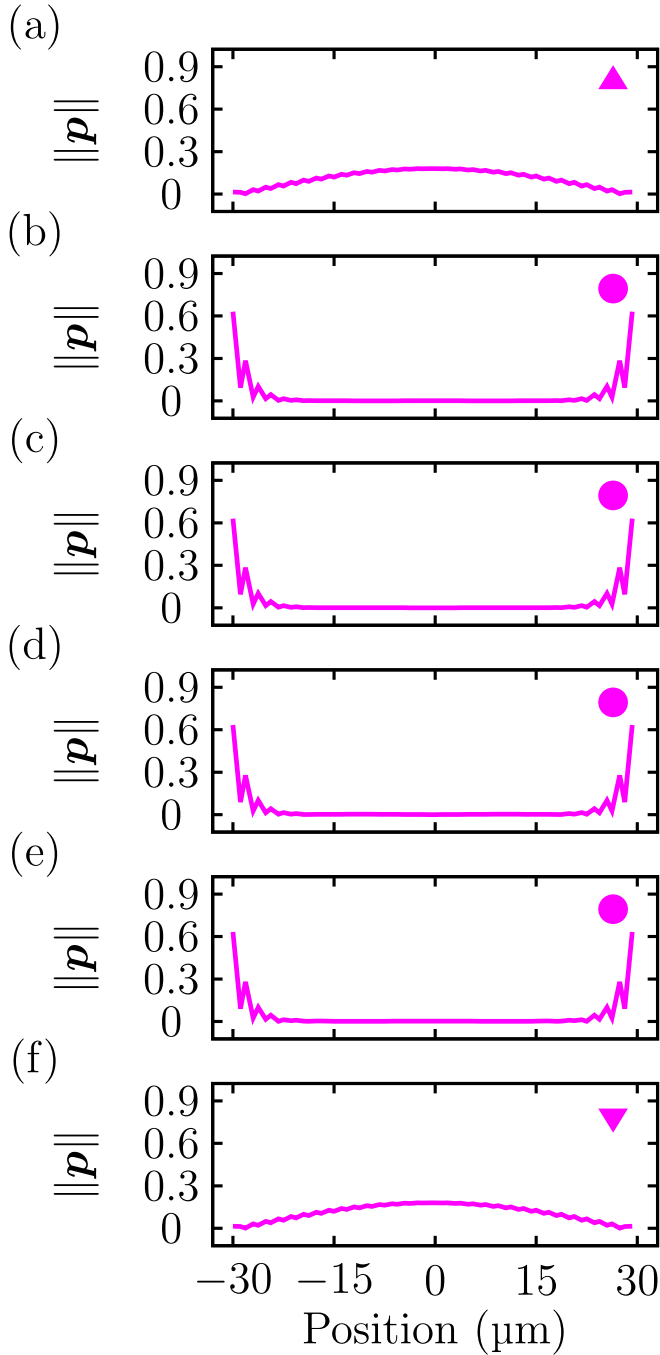


Figure 4.10: The norm of eigenmodes corresponding to the labeled modes in the band structures in Fig. 4.9. The results for the system with $\delta_L = -0.2$ and $\delta_R = -0.2$. (a), (f) are the upper and the lower bands, respectively. (b), (c), (d), (e) are topological edge modes and each of them has two-fold degeneracy.

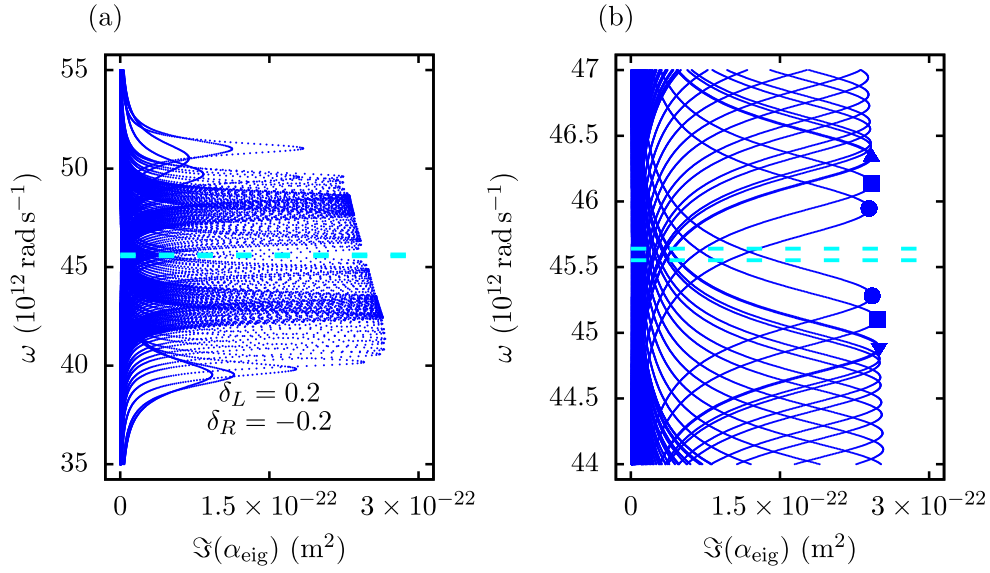


Figure 4.11: Band structures of dimer model of gyroelectric cylinders on 1D finite lattice with $B = 0.5 \text{ T}$. (a) The system with $\delta_L = 0.2$ and $\delta_R = -0.2$, where the left and the right part of the lattice are topologically trivial and non-trivial, respectively. (b) The same band structure in high resolution. The upper and the lower triangle indicate the upper and the lower bands, respectively. The circles and the squares are the topological edge modes. The cyan dashed line indicates the resonant frequency of a single gyroelectric cylinder $\omega_{0,\pm}$.

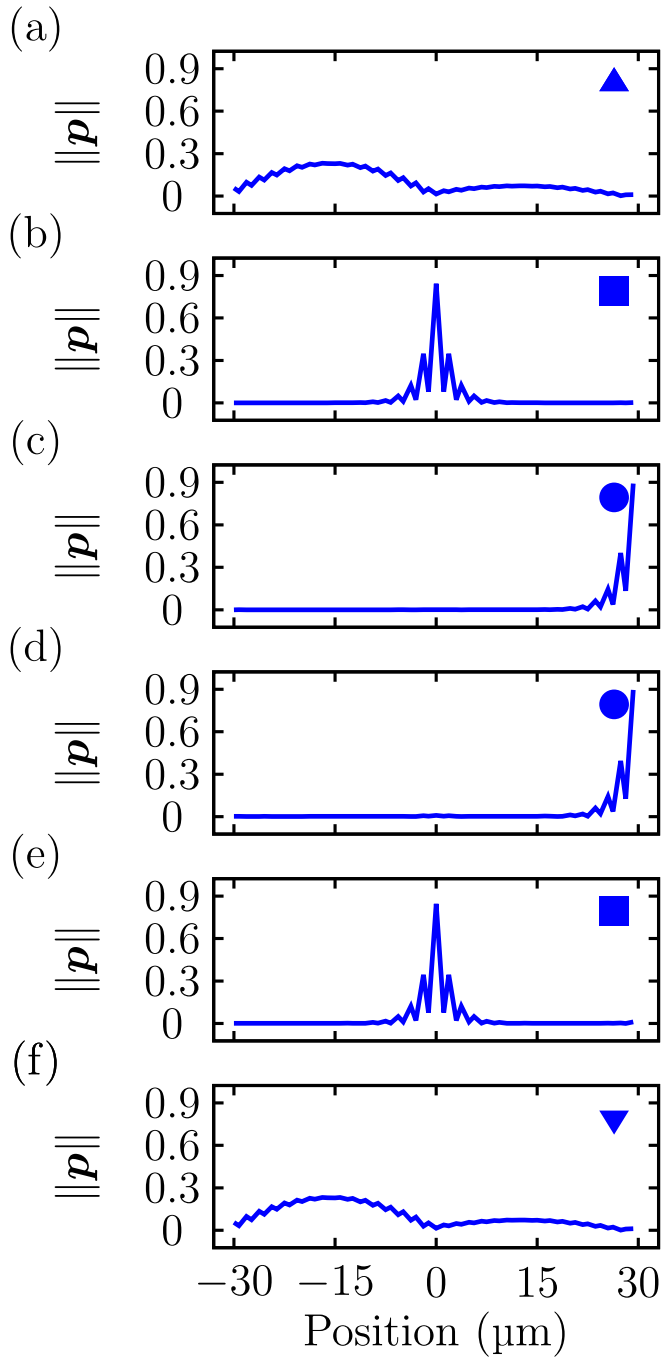


Figure 4.12: The norm of eigenmodes corresponding to the labeled modes in the band structures in Fig. 4.11. The results for the system with $\delta_L = 0.2$ and $\delta_R = -0.2$. (a), (f) are the upper and the lower bands, respectively. (b), (c), (d), (e) are topological edge modes.

radius $r = 2.5$ mm as depicted in Fig. 3.6. We assume there are N unit cells with N being an even number, so $n = -N/2, \dots, 0, \dots, N/2 - 1$. Then $n < 0$ corresponds to the left part and $n \geq 0$ corresponds to the right part of the lattice. The displacement from cylinder A to B in unit cell n is given by $\mathbf{b}_n = b_n \hat{\mathbf{x}}$, where

$$b_n = \begin{cases} b_L & \text{if } n < 0, \\ b_R & \text{if } n \geq 0, \end{cases} \quad (4.28)$$

with

$$b_L = \frac{a_2}{2}(1 - \delta_L), \quad (4.29a)$$

$$b_R = \frac{a_2}{2}(1 - \delta_R). \quad (4.29b)$$

In the n th unit cell, the electric dipole moments is $\mathbf{p}_n = (\mathbf{p}_{n,A}, \mathbf{p}_{n,B})^T$ and the polarizability is $\boldsymbol{\alpha}_n(\omega) = \text{diag}(\boldsymbol{\alpha}_{n,A}, \boldsymbol{\alpha}_{n,B})$. Then we have $\tilde{\mathbf{p}} = (\mathbf{p}_{-N/2}, \dots, \mathbf{p}_0, \dots, \mathbf{p}_{N/2-1})^T$ and $\tilde{\boldsymbol{\alpha}}(\omega) = \text{diag}(\boldsymbol{\alpha}_{-N/2}, \dots, \boldsymbol{\alpha}_0, \dots, \boldsymbol{\alpha}_{N/2-1})$. We define $\tilde{\boldsymbol{\Gamma}}(\omega)$ as the interactions between the unit cells i and unit cell j , such that for $i = j$,

$$\tilde{\boldsymbol{\Gamma}}_{ij} = \frac{k_0^2}{\epsilon_0} \begin{pmatrix} \mathbf{0} & \mathbf{G}(0, \mathbf{b}_i) \\ \mathbf{G}(0, -\mathbf{b}_i) & \mathbf{0} \end{pmatrix}, \quad (4.30)$$

and for $i \neq j$

$$\tilde{\Gamma}_{ij} = \frac{k_0^2}{\epsilon_0} \begin{pmatrix} \mathbf{G}(0, \mathbf{R}_{ij}) & \mathbf{G}(0, \mathbf{R}_{ij} + \mathbf{b}_i) \\ \mathbf{G}(0, \mathbf{R}_{ij} - \mathbf{b}_i) & \mathbf{G}(0, \mathbf{R}_{ij}) \end{pmatrix}, \quad (4.31)$$

where $\mathbf{R}_{ij} := (j - i)a_2\hat{\mathbf{x}}$ is the displacement from unit cell i to unit cell j . Furthermore, we define

$$\tilde{\mathbf{M}}_{\text{dimer}}(\omega) := \tilde{\boldsymbol{\alpha}}^{-1}(\omega) - \tilde{\Gamma}(\omega). \quad (4.32)$$

The coupled-dipole equations for the dimer model of gyromagnetic cylinders on 1D finite lattice can be written as

$$\tilde{\mathbf{M}}_{\text{dimer}}(\omega)\tilde{\mathbf{p}} = 0, \quad (4.33)$$

where $\tilde{\mathbf{M}}_{\text{dimer}}(\omega)$ is a $4N \times 4N$ matrix. Finally, we have the eigenvalue problem

$$\tilde{\mathbf{M}}_{\text{dimer}}(\omega)\tilde{\mathbf{p}}_i = \lambda_i(\omega)\tilde{\mathbf{p}}_i, \quad (4.34)$$

with eigen-response theory described in Sec. 2.4.

We consider the finite lattice with $N = 32$. First, we study the topological trivial case with both $\delta_L = 0.2$ and $\delta_R = 0.2$. This is the finite case of the dimer model studied in Sec. 4.2.1 with $\delta = 0.2$. To clearly show the eigenmodes, we plot the quantity $\Im(\alpha_{\text{eig}})$. The result is shown in Fig. 4.8 (a) and a high resolution plot is shown in Fig. 4.8 (b). We found that there are

two sets of modes correspond to the upper and the lower band of the system. There is no state within the band gap, as expected. The results are in good agreement with the band structure obtained in Fig. 4.5 (d).

Next, we consider the topological non-trivial case with both $\delta_L = -0.2$ and $\delta_R = -0.2$. As is well known from the conventional SSH model, this system should present topological edge modes at the end of the chain by the bulk-boundary correspondence. The result is shown in Fig. 4.9 (a) and a high resolution plot is shown in Fig. 4.9 (b). Again, we observed that there are two sets of modes correspond to the upper and the lower band of the system. The bottom of the upper band is labeled by the magenta upper triangle and the top of the lower band is labeled by the magenta lower triangle. However, in contrast to the trivial case, there are two localized mode in the band gap, which are two-fold degenerate and labeled by the magenta circle. Then we calculated the corresponding norm of the eigenmodes $\|\mathbf{p}\| = \sqrt{\mathbf{p}^* \mathbf{p}}$ of the system. For the localized modes in the band gap, the norm of the eigenmodes are shown in Fig. 4.12 (b), (c), (d), and (e). The localized modes have two-fold degeneracy. We see that, this eigenmode localized at $\mathbf{p}_{-N/2,A}$ and $\mathbf{p}_{N/2-1,B}$, which is at the end of the chain. This is the topological edge modes supporting in the system.

Furthermore, we choose the two extreme cases with $\delta_L = 0.2$ and $\delta_R = -0.2$. Then the left part of the lattice is in topological phase II, while the right part of the lattice is in topological phase I. The result is shown in Fig. 4.11 (a) and a high resolution plot is shown in Fig. 4.11 (b). Again, we

observed the upper and the lower band of the system, which are labeled by the upper blue triangle and the lower blue triangle, respectively. There are four localized modes in the band gap, which are labeled by blue circles and blue squares. There are four topological edge modes supporting in this system. For the localized mode labeled by blue circles, the norm of the eigenmode is shown in Fig. 4.12 (c) and (d). Now, this eigenmodes only localized at $\mathbf{p}_{N/2-1,B}$, which is the right end of the chain. For the localized mode labeled by blue squares, the norm of the eigenmode is shown in Fig. 4.12 (b) and (e). It is shown that, this eigenmode localized at $\mathbf{p}_{0,A}$, which is the boundary between the left and the right part of the lattice. As long as the left part and the right part of the lattice are in two distinct topological phases, protected modes exist at the boundary where there is topological phase transition.

In summary, we have studied the 1D array of strongly dispersive gyroelectric resonant cylinders in quasi-static limit and with dynamic long-range interactions. We find that, the results obtained in quasi-static limit already give good description to the qualitative features of the system. We showed that, studying the system in quasi-static limit is suffice to obtained a full band gap, as long as inversion symmetry is broken in the system. By considering a dimer model of gyroelectric cylinders on 1D finite lattice, we demonstrated topological edge modes supporting in 1D gyroelectric system. The topological edge modes are within four topological bands and can be understood by the bulk-boundary correspondence.

Conclusions

Topological photonics have been of great interest for the past decade and is a rapidly growing field of research, as the topological edge modes have promising applications. In this thesis, we studied one-dimensional (1D) topological gyrotropic lattices beyond the simplest topological model, which is the Su-Schrieffer-Heeger (SSH) model. Different from the tight-binding approach usually been used in photonic systems, we considered, in general, dispersive materials beyond the quasi-static limit.

In Chapter 3, we studied the dynamic long-range-interaction induced topological photonic edge modes in one-dimensional (1D) array of strongly dispersive gyromagnetic resonant cylinders. The longitudinal mode and the transverse mode are coupled and the normal modes of the system coupled strongly to the photon mode of the background medium. In the case of dimer lattices, we found that the creation of the non-trivial band gaps and topological edge modes rely on the dynamic long-range-interaction associated with the free-space photon modes of the background medium. Our results indicate that the dynamic long-range interaction plays a crucial role in predicting

the precise band structures and the spectral position of the topological edge modes in gyromagnetic systems.

In Chapter 4, we have studied the 1D array of strongly dispersive gyroelectric resonant cylinders in quasi-static limit and with dynamic long-range interactions. Different from the gyromagnetic lattice, we found that the results obtained in quasi-static limit already give good description to the qualitative features of the system. The longitudinal mode and the transverse mode of the system do not coupled together. We showed that, studying the system in quasi-static limit is sufficient to obtain a full band gap, as long as inversion symmetry is broken in the system. By considering a dimer model of gyroelectric cylinders on 1D finite lattice, we demonstrated topological edge modes supporting in 1D gyroelectric system. The topological edge modes are within four topological bands and can be understood by the bulk-boundary correspondence.

Our results indicate that the dynamic long-range interaction plays a crucial role in predicting the precise band structures and the spectral position of the topological edge modes in strongly dispersive gyrotropic systems, which deepen our understanding on the topology in non-reciprocal photonics.

Appendix A

Coupled-dipole equations in quasi-static limit

In quasi-static limit $k_0 \rightarrow 0$, the Hankel functions in Eq. (3.7) become[76]

$$H_0^{(1)}(k_0 R) \sim \frac{2i}{\pi} \ln k_0 R, \quad (\text{A.1a})$$

$$H_1^{(1)}(k_0 R) \sim -\frac{2i}{\pi} \left(\frac{1}{k_0 R} \right). \quad (\text{A.1b})$$

Hence, the 2D Green's tensor for our system in quasi-static limit is given by

$$\mathbf{G}'(\boldsymbol{\rho}, \boldsymbol{\rho}') = \begin{pmatrix} G'_{xx} & 0 \\ 0 & G'_{yy} \end{pmatrix}, \quad (\text{A.2})$$

with

$$G_{xx} = \frac{1}{2\pi} \frac{1}{(k_0 R)^2}, \quad (\text{A.3a})$$

$$G_{yy} = -\frac{1}{2\pi} \left(\ln k_0 R + \frac{1}{(k_0 R)^2} \right). \quad (\text{A.3b})$$

Now, \mathbf{G}' is real symmetric. Moreover, we define

$$\mathbf{A}(\boldsymbol{\rho}, \boldsymbol{\rho}') := \lim_{k_0 \rightarrow 0} 4\pi k_0^2 \mathbf{G}'(\boldsymbol{\rho}, \boldsymbol{\rho}'), \quad (\text{A.4})$$

and since $\lim_{k_0 \rightarrow 0} k_0^2 \ln k_0 R = 0$,

$$\mathbf{A}(\boldsymbol{\rho}, \boldsymbol{\rho}') = \begin{pmatrix} \frac{2}{R^2} & 0 \\ 0 & -\frac{2}{R^2} \end{pmatrix}. \quad (\text{A.5})$$

The polarizability in quasi-static limit $\boldsymbol{\alpha}'(\omega)$ is obtained by eliminating the radiative correction term in Eq. (4.1), as $\lim_{k_0 \rightarrow 0} -i(\pi k_0^2/2)\mathbf{I} = 0$. We have

$$\boldsymbol{\alpha}'^{-1}(\omega) = \frac{4}{r^2} \begin{pmatrix} \frac{\omega_h}{\omega_m} + \frac{1}{2} - i\beta \frac{\omega}{\omega_m} & i \frac{\omega}{\omega_m} \\ -i \frac{\omega}{\omega_m} & \frac{\omega_h}{\omega_m} + \frac{1}{2} - i\beta \frac{\omega}{\omega_m} \end{pmatrix}. \quad (\text{A.6})$$

Then the coupled-dipole equations in quasi-static limit are given by

$$\mathbf{m}(\boldsymbol{\rho}) = \boldsymbol{\alpha}'(\omega) \left(\sum_{\boldsymbol{\rho}' \neq \boldsymbol{\rho}} \mathbf{A}(\boldsymbol{\rho}, \boldsymbol{\rho}') \mathbf{m}(\boldsymbol{\rho}') + \mathbf{B}_0(\boldsymbol{\rho}) \right), \quad (\text{A.7})$$

and in the formalism of eigen-response theory, we define

$$\mathbf{M}'(\omega) := \boldsymbol{\alpha}'^{-1}(\omega) - \sum_{\boldsymbol{\rho}' \neq \boldsymbol{\rho}} \mathbf{A}(\boldsymbol{\rho}, \boldsymbol{\rho}'). \quad (\text{A.8})$$

For infinite lattice, with the Bloch's theorem in Eq. (3.9), Eq. (A.7) becomes

$$\mathbf{m}(\boldsymbol{\rho}) = \boldsymbol{\alpha}'(\omega) \left(\sum_{\mathbf{R} \neq 0} \mathbf{A}(0, \mathbf{R}) e^{i\mathbf{k} \cdot \mathbf{R}} \mathbf{m}(\boldsymbol{\rho}') + \mathbf{B}_0(\boldsymbol{\rho}) \right), \quad (\text{A.9})$$

then we define

$$\mathbf{M}'(\mathbf{k}, \omega) := \boldsymbol{\alpha}'^{-1}(\omega) - \sum_{\mathbf{R} \neq 0} \mathbf{A}(0, \mathbf{R}) e^{i\mathbf{k} \cdot \mathbf{R}}. \quad (\text{A.10})$$

It should be noted that, although \mathbf{A} is real symmetric, $\boldsymbol{\alpha}'$ is non-Hermitian, so \mathbf{M}' in both Eq. (A.8) and Eq. (A.10) are also non-Hermitian.

Appendix B

Coupled-dipole equations for the dimer model in quasi-static limit

We consider the dimer model in Sec. 3.2.1 in quasi-static limit, $k_0 \rightarrow 0$. The polarizability for cylinder A and cylinder B are given by Eq. (A.6) and are denoted by α'_A and α'_B , respectively. With the Bloch's theorem in Eq. (3.9) and with Eq. (A.5), the coupled-dipole equations for the dimer model can be written as

$$\begin{pmatrix} \alpha'_A{}^{-1} & 0 \\ 0 & \alpha'_B{}^{-1} \end{pmatrix} \begin{pmatrix} \mathbf{m}_A \\ \mathbf{m}_B \end{pmatrix} = \mathbf{\Gamma}' \begin{pmatrix} \mathbf{m}_A \\ \mathbf{m}_B \end{pmatrix}, \quad (\text{B.1})$$

APPENDIX B. COUPLED-DIPOLE EQUATIONS FOR THE DIMER MODEL IN QUASI-STAT

where we have defined

$$\mathbf{\Gamma}' := \begin{pmatrix} \sum_{\mathbf{R} \neq 0} \mathbf{A}(0, \mathbf{R}) e^{i\mathbf{k} \cdot \mathbf{R}} & \sum_{\mathbf{R}} \mathbf{A}(0, \mathbf{R} + \mathbf{b}) e^{i\mathbf{k} \cdot \mathbf{R}} \\ \sum_{\mathbf{R}} \mathbf{A}(0, \mathbf{R} - \mathbf{b}) e^{i\mathbf{k} \cdot \mathbf{R}} & \sum_{\mathbf{R} \neq 0} \mathbf{A}(0, \mathbf{R}) e^{i\mathbf{k} \cdot \mathbf{R}} \end{pmatrix}. \quad (\text{B.2})$$

It should be noted that, since \mathbf{A} is real symmetric, $\mathbf{\Gamma}'$ is Hermitian. In the formalism of eigen-response theory, we define

$$\mathbf{M}'_{\text{dimer}}(\mathbf{k}, \omega) := \begin{pmatrix} \boldsymbol{\alpha}'_A^{-1} & 0 \\ 0 & \boldsymbol{\alpha}'_B^{-1} \end{pmatrix} - \mathbf{\Gamma}'. \quad (\text{B.3})$$

Now, since $\boldsymbol{\alpha}'$ is non-Hermitian, \mathbf{M}' is also non-Hermitian.

Appendix C

Finite gyromagnetic lattice in quasi-static limit

The band structures of dimer model of gyromagnetic cylinders on 1D finite lattice in quasi-static limit are shown in Fig. C.1. The norm of the localized eigenmodes corresponding to the band structures in Fig. C.1 are shown in Fig. C.2. From the results, we see that, apart from not having a full band gap, the resonant frequency of a single gyromagnetic cylinder ω_0 , which corresponds to the zero-energy state in the SSH model, is on top of the bands. Although topological non-trivial edge modes may exist even in absence of a band gap, the spectral positions of the edge modes still lie within two topological bands and can be understood by the bulk-boundary correspondence[44]. In our case, since the chiral symmetry ensures the spectral position of any edge modes lies at ω_0 , the topological nature of edge

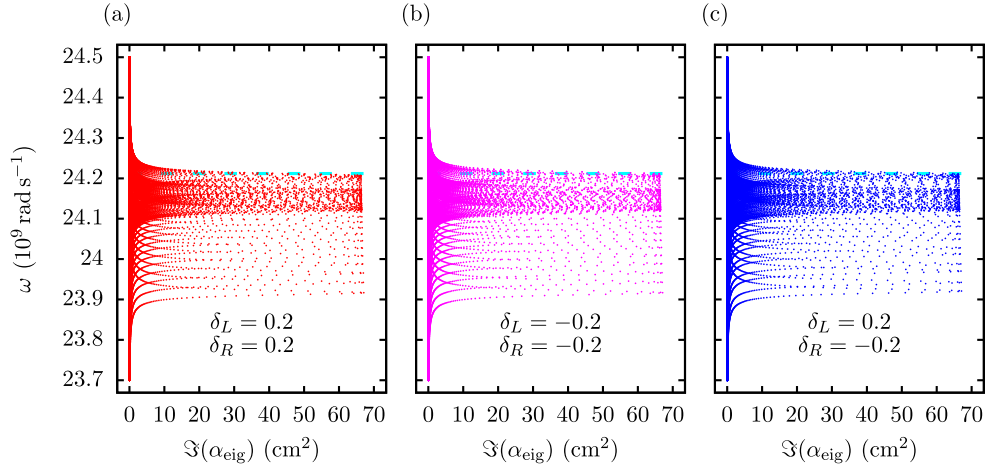


Figure C.1: Band structures of dimer model of gyromagnetic cylinders on 1D finite lattice in quasi-static limit. (a) The system with both $\delta_L = 0.2$ and $\delta_R = 0.2$. (b) The system with both $\delta_L = -0.2$ and $\delta_R = -0.2$. (c) The system with $\delta_L = 0.2$ and $\delta_R = -0.2$. The cyan dashed line indicates the resonant frequency of a single gyromagnetic cylinder ω_0 .

mode is not well defined.

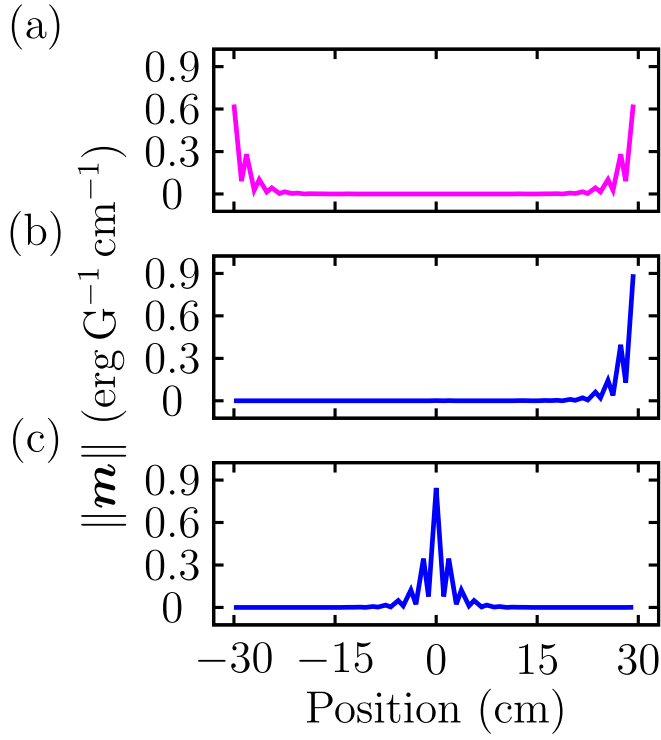


Figure C.2: The norm of the localized eigenmodes corresponding to the band structures in Fig. C.1. (a) The results for the system with $\delta_L = -0.2$ and $\delta_R = -0.2$ at $\omega = 24.2112 \times 10^9 \text{ rad s}^{-1}$. (b), (c) The results for the system with $\delta_L = 0.2$ and $\delta_R = -0.2$ at $\omega = 24.2112 \times 10^9 \text{ rad s}^{-1}$ and $\omega = 24.2096 \times 10^9 \text{ rad s}^{-1}$.

References

- [1] Mark L Brongersma, John W Hartman, and Harry A Atwater. Electromagnetic energy transfer and switching in nanoparticle chain arrays below the diffraction limit. *Physical Review B*, 62(24):R16356, 2000.
- [2] Romain Quidant, Christian Girard, Jean-Claude Weeber, and Alain Dereux. Tailoring the transmittance of integrated optical waveguides with short metallic nanoparticle chains. *Physical Review B*, 69(8):085407, 2004.
- [3] Britain Willingham and Stephan Link. Energy transport in metal nanoparticle chains via sub-radiant plasmon modes. *Optics Express*, 19(7):6450–6461, 2011.
- [4] Kin Hung Fung and C. T. Chan. Plasmonic modes in periodic metal nanoparticle chains: a direct dynamic eigenmode analysis. *Opt. Lett.*, 32(8):973–975, Apr 2007. doi: 10.1364/OL.32.000973. URL <http://ol.osa.org/abstract.cfm?URI=ol-32-8-973>.
- [5] W. H. Weber and G. W. Ford. Propagation of optical excitations by

- dipolar interactions in metal nanoparticle chains. *Phys. Rev. B*, 70:125429, Sep 2004. doi: 10.1103/PhysRevB.70.125429. URL <https://link.aps.org/doi/10.1103/PhysRevB.70.125429>.
- [6] Nicholas A Pike and David Stroud. Spin waves on chains of yig particles: dispersion relations, faraday rotation, and power transmission. *The European Physical Journal B*, 90(3):59, 2017.
- [7] Zhen Li, Rui xin Wu, Qing bo Li, and Yin Poo. Realization of self-guided unidirectional waveguides by a chain of gyromagnetic rods. *Appl. Opt.*, 54(6):1267–1272, Feb 2015. doi: 10.1364/AO.54.001267. URL <http://ao.osa.org/abstract.cfm?URI=ao-54-6-1267>.
- [8] Nanfang Yu, Patrice Genevet, Mikhail A Kats, Francesco Aieta, Jean-Philippe Tetienne, Federico Capasso, and Zeno Gaburro. Light propagation with phase discontinuities: generalized laws of reflection and refraction. *science*, 334(6054):333–337, 2011.
- [9] KL Tsakmakidis, L Shen, SA Schulz, X Zheng, J Upham, X Deng, H Altug, Alexander F Vakakis, and RW Boyd. Breaking lorentz reciprocity to overcome the time-bandwidth limit in physics and engineering. *Science*, 356(6344):1260–1264, 2017.
- [10] Dirk Jalas, Alexander Petrov, Manfred Eich, Wolfgang Freude, Shanhui Fan, Zongfu Yu, Roel Baets, Miloš Popović, Andrea Melloni, John D

- Joannopoulos, et al. What is—and what is not—an optical isolator. *Nature Photonics*, 7(8):579, 2013.
- [11] AC Mahoney, JI Colless, SJ Pauka, JM Hornibrook, JD Watson, GC Gardner, MJ Manfra, AC Doherty, and DJ Reilly. On-chip microwave quantum hall circulator. *Physical Review X*, 7(1):011007, 2017.
- [12] Y Hadad and Ben Z Steinberg. Magnetized spiral chains of plasmonic ellipsoids for one-way optical waveguides. *Physical review letters*, 105(23):233904, 2010.
- [13] CW Ling, Jin Wang, and Kin Hung Fung. Formation of nonreciprocal bands in magnetized diatomic plasmonic chains. *Physical Review B*, 92(16):165430, 2015.
- [14] Ling Lu, John D Joannopoulos, and Marin Soljačić. Topological photonics. *Nat. Photon.*, 8(11):821, 2014.
- [15] Tomoki Ozawa, Hannah M. Price, Alberto Amo, Nathan Goldman, Mohammad Hafezi, Ling Lu, Mikael C. Rechtsman, David Schuster, Jonathan Simon, Oded Zilberberg, and Iacopo Carusotto. Topological photonics. *Rev. Mod. Phys.*, 91:015006, Mar 2019. doi: 10.1103/RevModPhys.91.015006. URL <https://link.aps.org/doi/10.1103/RevModPhys.91.015006>.
- [16] F. D. M. Haldane and S. Raghu. Possible realization of directional optical waveguides in photonic crystals with broken time-reversal symmetry.

- Phys. Rev. Lett.*, 100:013904, Jan 2008. doi: 10.1103/PhysRevLett.100.013904. URL <https://link.aps.org/doi/10.1103/PhysRevLett.100.013904>.
- [17] Zheng Wang, Y. D. Chong, John D. Joannopoulos, and Marin Soljačić. Reflection-free one-way edge modes in a gyromagnetic photonic crystal. *Phys. Rev. Lett.*, 100:013905, Jan 2008. doi: 10.1103/PhysRevLett.100.013905. URL <https://link.aps.org/doi/10.1103/PhysRevLett.100.013905>.
- [18] S. Raghu and F. D. M. Haldane. Analogs of quantum-hall-effect edge states in photonic crystals. *Phys. Rev. A*, 78:033834, Sep 2008. doi: 10.1103/PhysRevA.78.033834. URL <https://link.aps.org/doi/10.1103/PhysRevA.78.033834>.
- [19] Zheng Wang, Yidong Chong, John D Joannopoulos, and Marin Soljačić. Observation of unidirectional backscattering-immune topological electromagnetic states. *Nature*, 461(7265):772, 2009.
- [20] Kejie Fang, Zongfu Yu, and Shanhui Fan. Microscopic theory of photonic one-way edge mode. *Phys. Rev. B*, 84:075477, Aug 2011. doi: 10.1103/PhysRevB.84.075477. URL <https://link.aps.org/doi/10.1103/PhysRevB.84.075477>.
- [21] Mohammad Hafezi, Eugene A Demler, Mikhail D Lukin, and Jacob M

- Taylor. Robust optical delay lines with topological protection. *Nat. Phys.*, 7(11):907, 2011.
- [22] Mohammad Hafezi, S Mittal, J Fan, A Migdall, and JM Taylor. Imaging topological edge states in silicon photonics. *Nat. Photon.*, 7(12):1001, 2013.
- [23] Alexander B Khanikaev, S Hossein Mousavi, Wang-Kong Tse, Mehdi Kargarian, Allan H MacDonald, and Gennady Shvets. Photonic topological insulators. *Nat. Mater.*, 12(3):233, 2013.
- [24] Long-Hua Wu and Xiao Hu. Scheme for achieving a topological photonic crystal by using dielectric material. *Phys. Rev. Lett.*, 114:223901, Jun 2015. doi: 10.1103/PhysRevLett.114.223901. URL <https://link.aps.org/doi/10.1103/PhysRevLett.114.223901>.
- [25] Jia Ningyuan, Clai Owens, Ariel Sommer, David Schuster, and Jonathan Simon. Time- and site-resolved dynamics in a topological circuit. *Phys. Rev. X*, 5:021031, Jun 2015. doi: 10.1103/PhysRevX.5.021031. URL <https://link.aps.org/doi/10.1103/PhysRevX.5.021031>.
- [26] Brandon M. Anderson, Ruichao Ma, Clai Owens, David I. Schuster, and Jonathan Simon. Engineering topological many-body materials in microwave cavity arrays. *Phys. Rev. X*, 6:041043, Dec 2016. doi: 10.1103/PhysRevX.6.041043. URL <https://link.aps.org/doi/10.1103/PhysRevX.6.041043>.

- [27] Clai Owens, Aman LaChapelle, Brendan Saxberg, Brandon M. Anderson, Ruichao Ma, Jonathan Simon, and David I. Schuster. Quarter-flux hofstadter lattice in a qubit-compatible microwave cavity array. *Phys. Rev. A*, 97:013818, Jan 2018. doi: 10.1103/PhysRevA.97.013818. URL <https://link.aps.org/doi/10.1103/PhysRevA.97.013818>.
- [28] Ling Lu, Liang Fu, John D Joannopoulos, and Marin Soljačić. Weyl points and line nodes in gyroid photonic crystals. *Nat. Photon.*, 7(4):294, 2013.
- [29] Xi-Wang Luo, Xingxiang Zhou, Chuan-Feng Li, Jin-Shi Xu, Guang-Can Guo, and Zheng-Wei Zhou. Quantum simulation of 2d topological physics in a 1d array of optical cavities. *Nat. Commun.*, 6:7704, 2015.
- [30] Oded Zilberberg, Sheng Huang, Jonathan Guglielmon, Mohan Wang, Kevin P Chen, Yaacov E Kraus, and Mikael C Rechtsman. Photonic topological boundary pumping as a probe of 4d quantum hall physics. *Nature*, 553(7686):59, 2018.
- [31] P St-Jean, V Goblot, E Galopin, A Lemaître, T Ozawa, L Le Gratiet, I Sagnes, J Bloch, and A Amo. Lasing in topological edge states of a one-dimensional lattice. *Nat. Photon.*, 11(10):651, 2017.
- [32] Babak Bahari, Abdoulaye Ndao, Felipe Vallini, Abdelkrim El Amili, Yeshaiahu Fainman, and Boubacar Kanté. Nonreciprocal lasing in topological cavities of arbitrary geometries. *Science*, 358(6363):636–

- 640, 2017. ISSN 0036-8075. doi: 10.1126/science.aao4551. URL <http://science.sciencemag.org/content/358/6363/636>.
- [33] Han Zhao, Pei Miao, Mohammad H Teimourpour, Simon Malzard, Ramy El-Ganainy, Henning Schomerus, and Liang Feng. Topological hybrid silicon microlasers. *Nat. Commun.*, 9(1):981, 2018.
- [34] Midya Parto, Steffen Wittek, Hossein Hodaei, Gal Harari, Miguel A. Bandres, Jinhan Ren, Mikael C. Rechtsman, Mordechai Segev, Demetrios N. Christodoulides, and Mercedeh Khajavikhan. Edge-mode lasing in 1d topological active arrays. *Phys. Rev. Lett.*, 120:113901, Mar 2018. doi: 10.1103/PhysRevLett.120.113901. URL <https://link.aps.org/doi/10.1103/PhysRevLett.120.113901>.
- [35] Gal Harari, Miguel A. Bandres, Yaakov Lumer, Mikael C. Rechtsman, Y. D. Chong, Mercedeh Khajavikhan, Demetrios N. Christodoulides, and Mordechai Segev. Topological insulator laser: Theory. *Science*, 359(6381), 2018. ISSN 0036-8075. doi: 10.1126/science.aar4003. URL <http://science.sciencemag.org/content/359/6381/eaar4003>.
- [36] Miguel A. Bandres, Steffen Wittek, Gal Harari, Midya Parto, Jinhan Ren, Mordechai Segev, Demetrios N. Christodoulides, and Mercedeh Khajavikhan. Topological insulator laser: Experiments. *Science*, 359(6381), 2018. ISSN 0036-8075. doi: 10.1126/science.aar4005. URL <http://science.sciencemag.org/content/359/6381/eaar4005>.

- [37] Robert Keil, Julia M Zeuner, Felix Dreisow, Matthias Heinrich, Andreas Tünnermann, Stefan Nolte, and Alexander Szameit. The random mass dirac model and long-range correlations on an integrated optical platform. *Nat. Commun.*, 4:1368, 2013.
- [38] Meng Xiao, Z. Q. Zhang, and C. T. Chan. Surface impedance and bulk band geometric phases in one-dimensional systems. *Phys. Rev. X*, 4:021017, Apr 2014. doi: 10.1103/PhysRevX.4.021017. URL <https://link.aps.org/doi/10.1103/PhysRevX.4.021017>.
- [39] Alexander Poddubny, Andrey Miroshnichenko, Alexey Slobozhanyuk, and Yuri Kivshar. Topological majorana states in zigzag chains of plasmonic nanoparticles. *ACS Photonics*, 1(2):101–105, 2014. doi: 10.1021/ph4000949. URL <https://doi.org/10.1021/ph4000949>.
- [40] C. W. Ling, Meng Xiao, C. T. Chan, S. F. Yu, and K. H. Fung. Topological edge plasmon modes between diatomic chains of plasmonic nanoparticles. *Opt. Express*, 23(3):2021–2031, Feb 2015. doi: 10.1364/OE.23.002021. URL <http://www.opticsexpress.org/abstract.cfm?URI=oe-23-3-2021>.
- [41] Ivan S. Sinev, Ivan S. Mukhin, Alexey P. Slobozhanyuk, Alexander N. Poddubny, Andrey E. Miroshnichenko, Anton K. Samusev, and Yuri S. Kivshar. Mapping plasmonic topological states at the nanoscale. *Nanoscale*, 7:11904–11908, 2015. doi: 10.1039/C5NR00231A. URL <http://dx.doi.org/10.1039/C5NR00231A>.

- [42] Charles A. Downing and Guillaume Weick. Topological collective plasmons in bipartite chains of metallic nanoparticles. *Phys. Rev. B*, 95:125426, Mar 2017. doi: 10.1103/PhysRevB.95.125426. URL <https://link.aps.org/doi/10.1103/PhysRevB.95.125426>.
- [43] Yong-Liang Zhang, Raymond P. H. Wu, Anshuman Kumar, Tiejian Si, and Kin Hung Fung. Nonsymmorphic symmetry-protected topological modes in plasmonic nanoribbon lattices. *Phys. Rev. B*, 97:144203, Apr 2018. doi: 10.1103/PhysRevB.97.144203. URL <https://link.aps.org/doi/10.1103/PhysRevB.97.144203>.
- [44] Simon R. Pockock, Xiaofei Xiao, Paloma A. Huidobro, and Vincenzo Giannini. Topological plasmonic chain with retardation and radiative effects. *ACS Photonics*, 5(6):2271–2279, 2018. doi: 10.1021/acsp Photonics.8b00117. URL <https://doi.org/10.1021/acsp Photonics.8b00117>.
- [45] Charles A. Downing and Guillaume Weick. Topological plasmons in dimerized chains of nanoparticles: robustness against long-range quasistatic interactions and retardation effects. *Eur. Phys. J. B*, 91(10):253, Oct 2018. ISSN 1434-6036. doi: 10.1140/epjb/e2018-90199-0. URL <https://doi.org/10.1140/epjb/e2018-90199-0>.
- [46] Alexey P. Slobozhanyuk, Alexander N. Poddubny, Andrey E. Miroshnichenko, Pavel A. Belov, and Yuri S. Kivshar. Subwavelength topological edge states in optically resonant dielectric structures. *Phys.*

- Rev. Lett.*, 114:123901, Mar 2015. doi: 10.1103/PhysRevLett.114.123901. URL <https://link.aps.org/doi/10.1103/PhysRevLett.114.123901>.
- [47] Alexey P. Slobozhanyuk, Alexander N. Poddubny, Ivan S. Sinev, Anton K. Samusev, Ye Feng Yu, Arseniy I. Kuznetsov, Andrey E. Miroshnichenko, and Yuri S. Kivshar. Enhanced photonic spin hall effect with subwavelength topological edge states. *Laser Photonics Rev.*, 10(4):656–664, 2016. doi: 10.1002/lpor.201600042. URL <https://onlinelibrary.wiley.com/doi/abs/10.1002/lpor.201600042>.
- [48] Sergey Kruk, Alexey Slobozhanyuk, Denitza Denkova, Alexander Poddubny, Ivan Kravchenko, Andrey Miroshnichenko, Dragomir Neshev, and Yuri Kivshar. Edge states and topological phase transitions in chains of dielectric nanoparticles. *Small*, 13(11):1603190, 2017. doi: 10.1002/smll.201603190. URL <https://onlinelibrary.wiley.com/doi/abs/10.1002/smll.201603190>.
- [49] Mário G Silveirinha. Chern invariants for continuous media. *Physical Review B*, 92(12):125153, 2015.
- [50] Seyyed Ali Hassani Gangaraj and George W Hanson. Topologically protected unidirectional surface states in biased ferrites: duality and application to directional couplers. *IEEE Antennas and Wireless Propagation Letters*, 16:449–452, 2016.

- [51] Xianyu Ao, Zhifang Lin, and C. T. Chan. One-way edge mode in a magneto-optical honeycomb photonic crystal. *Phys. Rev. B*, 80:033105, Jul 2009. doi: 10.1103/PhysRevB.80.033105. URL <https://link.aps.org/doi/10.1103/PhysRevB.80.033105>.
- [52] Yin Poo, Rui-xin Wu, Zhifang Lin, Yan Yang, and CT Chan. Experimental realization of self-guiding unidirectional electromagnetic edge states. *Physical Review Letters*, 106(9):093903, 2011.
- [53] Ara A. Asatryan, Lindsay C. Botten, Kejie Fang, Shanhui Fan, and Ross C. McPhedran. Local density of states of chiral hall edge states in gyrotropic photonic clusters. *Phys. Rev. B*, 88:035127, Jul 2013. doi: 10.1103/PhysRevB.88.035127. URL <https://link.aps.org/doi/10.1103/PhysRevB.88.035127>.
- [54] Zhen Li, Rui-xin Wu, Qing-Bo Li, Zhi-fang Lin, Yin Poo, Rong-Juan Liu, and Zhi-Yuan Li. Observation of broadband unidirectional transmission by fusing the one-way edge states of gyromagnetic photonic crystals. *Optics Express*, 23(8):9658–9663, 2015.
- [55] W. P. Su, J. R. Schrieffer, and A. J. Heeger. Solitons in polyacetylene. *Phys. Rev. Lett.*, 42:1698–1701, Jun 1979. doi: 10.1103/PhysRevLett.42.1698. URL <https://link.aps.org/doi/10.1103/PhysRevLett.42.1698>.
- [56] János K Asbóth, László Oroszlány, and András Pályi. *The Su-Schrieffer-*

- Heeger (SSH) Model*, volume 919 of *Lecture Notes in Physics*, pages 1–22. Springer, 2016.
- [57] David J. Bergman and D. Stroud. Theory of resonances in the electromagnetic scattering by macroscopic bodies. *Phys. Rev. B*, 22:3527–3539, Oct 1980. doi: 10.1103/PhysRevB.22.3527. URL <https://link.aps.org/doi/10.1103/PhysRevB.22.3527>.
- [58] Vadim A. Markel. Antisymmetrical optical states. *J. Opt. Soc. Am. B*, 12(10):1783–1791, Oct 1995. doi: 10.1364/JOSAB.12.001783. URL <http://josab.osa.org/abstract.cfm?URI=josab-12-10-1783>.
- [59] Kin Hung Fung and C. T. Chan. Analytical study of the plasmonic modes of a metal nanoparticle circular array. *Phys. Rev. B*, 77:205423, May 2008. doi: 10.1103/PhysRevB.77.205423. URL <https://link.aps.org/doi/10.1103/PhysRevB.77.205423>.
- [60] Lukas Novotny and Bert Hecht. *Theoretical foundations*, pages 12–44. Cambridge University Press, 2 edition, 2012. doi: 10.1017/CBO9780511794193.004.
- [61] Olivier J. F. Martin and Nicolas B. Piller. Electromagnetic scattering in polarizable backgrounds. *Phys. Rev. E*, 58:3909–3915, Sep 1998. doi: 10.1103/PhysRevE.58.3909. URL <https://link.aps.org/doi/10.1103/PhysRevE.58.3909>.

- [62] Salvatore Campione and Filippo Capolino. Ewald method for 3d periodic dyadic green's functions and complex modes in composite materials made of spherical particles under the dual dipole approximation. *Radio Science*, 47(6), 2012. doi: 10.1029/2012RS005031. URL <https://agupubs.onlinelibrary.wiley.com/doi/abs/10.1029/2012RS005031>.
- [63] J Zak. Berry's phase for energy bands in solids. *Physical review letters*, 62(23):2747, 1989.
- [64] AM Marques and RG Dias. Generalization of zak's phase for lattice models with non-centered inversion symmetry axis. *arXiv preprint arXiv:1707.06162*, 2017.
- [65] Jun-Won Rhim, Jan Behrends, and Jens H Bardarson. Bulk-boundary correspondence from the intercellular zak phase. *Physical Review B*, 95(3):035421, 2017.
- [66] P. C. Chaumet and M. Nieto-Vesperinas. Coupled dipole method determination of the electromagnetic force on a particle over a flat dielectric substrate. *Phys. Rev. B*, 61:14119–14127, May 2000. doi: 10.1103/PhysRevB.61.14119. URL <https://link.aps.org/doi/10.1103/PhysRevB.61.14119>.
- [67] D. M. Bolle and L. Lewin. On the definitions of parameters in ferrite-electromagnetic wave interactions (letters). *IEEE Trans. Mi-*

- crow. Theory Techn.*, 21(2):118–118, Feb 1973. ISSN 0018-9480. doi: 10.1109/TMTT.1973.1127939.
- [68] David M Pozar. *Theory and Design of Ferrimagnetic Components*, pages 451–495. John Wiley & Sons, 4 edition, 2009.
- [69] John D. Joannopoulos, Steven G. Johnson, Joshua N. Winn, and Robert D. Meade. *Symmetries and Solid-State Electromagnetism*, pages 25–43. Princeton University Press, 2 edition, 2008.
- [70] Marcos Atala, Monika Aidelsburger, Julio T Barreiro, Dmitry Abanin, Takuya Kitagawa, Eugene Demler, and Immanuel Bloch. Direct measurement of the zak phase in topological bloch bands. *Nat. Phys.*, 9(12): 795, 2013.
- [71] Meng Xiao, Guancong Ma, Zhiyu Yang, Ping Sheng, ZQ Zhang, and Che Ting Chan. Geometric phase and band inversion in periodic acoustic systems. *Nat. Phys.*, 11(3):240, 2015.
- [72] S. L. McCall, P. M. Platzman, R. Dalichaouch, David Smith, and S. Schultz. Microwave propagation in two-dimensional dielectric lattices. *Phys. Rev. Lett.*, 67:2017–2020, Oct 1991. doi: 10.1103/PhysRevLett.67.2017. URL <https://link.aps.org/doi/10.1103/PhysRevLett.67.2017>.
- [73] W. M. Robertson, G. Arjavalingam, R. D. Meade, K. D. Brommer, A. M. Rappe, and J. D. Joannopoulos. Measurement of photonic band struc-

- ture in a two-dimensional periodic dielectric array. *Phys. Rev. Lett.*, 68:2023–2026, Mar 1992. doi: 10.1103/PhysRevLett.68.2023. URL <https://link.aps.org/doi/10.1103/PhysRevLett.68.2023>.
- [74] Qiang Cheng, XM Yang, HF Ma, JY Chin, TJ Cui, R Liu, and DR Smith. Experiments and applications of metamaterials in microwave regime. In *Metamaterials*, pages 321–355. Springer, 2010.
- [75] P Halevi, , and F Ramos-Mendieta. Tunable photonic crystals with semiconducting constituents. *physical Review letters*, 85(9):1875, 2000.
- [76] Mary L Boas. *Series Solutions of Differential Equations; Legendre, Bessel, Hermite, and Laguerre Functions*, pages 562–618. John Wiley & Sons, 3 edition, 2006.